----------------REVISION 1----------------

Regular Article
Word Count: 9326 through Acknowledgements

Reconstructing diagenetic mineral reactions from silicified horizons of the Paleoproterozoic Biwabik Iron Formation, Minnesota

Samuel Duncanson*[1, 2], Latisha Brengman[1], Jena Johnson[3], Athena Eyster[4], John Fournelle[4], Aurélien Moy[4]

[1] Department of Earth and Environmental Sciences, University of Minnesota – Duluth, Duluth, MN, 55812, [2]Now at Department of Geological and Atmospheric Sciences, Iowa State University, Ames, IA 50011, [3] Department of Earth and Environmental Sciences, University of Michigan, Ann Arbor, MI 48109, [4] Department of Geoscience, University of Wisconsin Madison, Madison, WI 53706.

Email addresses: sdunc@iastate.edu* (SD) , lbrenmga@d.umn.edu (LB) , jenaje@umich.edu (JJ), aeyster@wisc.edu (AE), johnf@geology.wisc.edu (JF), amoy6@wisc.edu (AM)

Corresponding Author*: Sam Duncanson, Department of Geological and Atmospheric Sciences, Iowa State University, Ames, Iowa 50011 USA, Phone: 515-294-4477, Email: sdunc@iastate.edu

Keywords:
silicification, silica cementation, diagenesis, chamosite, greenalite

ABSTRACT

Primary phases in iron-rich chemical sedimentary rocks are important archives of seawater geochemistry throughout the Precambrian. The record of seawater chemistry, however, is obscured by post-depositional changes that occur during diagenesis, metamorphism, and modern weathering. Recent studies have identified silica-cemented horizons in some Archean and Paleoproterozoic iron formation that may preserve reduced, texturally early mineral phases, which may inform interpretations of oxygen dynamics preceding atmospheric oxygen accumulation before the ~2.3 Ga Great Oxidation Event (GOE). However, fewer investigations focus on silica-cemented horizons in Paleoproterozoic iron formation deposited after the GOE, a period where oxygen levels are poorly constrained. Here we present petrographic observations, scanning electron microscopy, electron microprobe analysis, and Raman spectroscopy from iron mineral phases preserved within silica-cemented horizons of the ~1.9 Ga Biwabik Iron Formation (Minnesota, United States) to constrain texturally early iron formation mineralogy from this crucial post-GOE interval. Based on textural relationships, the iron silicate greenalite is identified as the earliest-forming iron silicate mineral preserved within silica-cemented horizons. The magnesium- and aluminum-rich iron silicates chamosite and stilpnomelane are preserved proximal to fine-grained, non-silicified horizons, suggesting local geochemical exchange during early diagenesis. The presence of well-preserved, early-forming silicates containing predominantly ferrous iron may indicate reducing conditions at the sediment-water interface during deposition of the Biwabik Iron Formation. More definitively, future studies using iron silicate mineralogy as seawater geochemistry proxies should consider preservation by silica cementation, in addition to the effects of local geochemical exchange during diagenesis.

INTRODUCTION

Chemical sedimentary rocks, such as iron formations, archive geochemical conditions of marine environments throughout Earth history. Iron formations are iron and silica-rich chemical sedimentary rocks deposited throughout the Precambrian sedimentary record, notable for providing a record of marine (bio)geochemistry across the Archean-Proterozoic transition and the initial rise of atmospheric oxygen concentrations during the ~2.2-2.4 Ga Great Oxidation Event (GOE; Lyons et al. 2014; Gumsley et al. 2017; Poulton et al. 2021). Primary authigenic phases preserved in iron formations are of interest because they may record critical chemical information about the water column. Here, primary phases are defined as the earliest forming minerals that reflect geochemical conditions of the fluid at their time of precipitation. Following deposition, primary phases experience processes that alter and overprint original geochemical signatures including early and late diagenesis, burial, metasomatism and metamorphism, and modern weathering during fluid permeation and surface exposure (Klein 2005; Albut et al. 2018). Deciphering the mineralization histories and distinguishing these later secondary and tertiary mineral phases from primary phases is crucial for elucidating original geochemical information that can be linked to the depositing fluid and original depositional conditions.

Cementation by silica during early diagenesis may aid in mineral preservation by encapsulating precursor sediments near the time of silica precipitation, preventing subsequent major cation exchange and mineral transformations (Simonson 1987). Favorably, throughout most of the Precambrian, the lack of silica biomineral sinks likely resulted in high seawater silica concentrations at or above saturation (e.g., Siever 1992; Maliva et al. 2005), evidenced in part by deposition of abundant Si-rich chemical sedimentary rocks and widespread silicification (e.g., Brengman et al. 2020). Recent studies of silica-cemented horizons in iron formation identified iron silicate inclusions, specifically Fe(II)-rich greenalite, and interpreted these minerals as primary precipitates reflective of anoxic depositional conditions (Rasmussen et al. 2013; Johnson et al. 2018; Muhling and Rasmussen 2020; Rasmussen et al. 2021 and references therein). The presence of putative primary greenalite within these silica-cemented horizons, when paired with laboratory synthesis of greenalite, suggests Fe(II)-rich and very low oxygen conditions were required to produce the earliest-forming minerals constituting iron formations (Tosca et al. 2016; Jiang and Tosca 2019; Hinz et al. 2021). These discoveries therefore represent a challenge to the longstanding model of a primary iron-oxide pathway of iron formation genesis where ferrous iron oxidizes and precipitates via interaction with oxygen, light, and/or microorganisms (Konhauser et al. 2017). Indeed, a new model of iron formation genesis has emerged wherein Fe(II) and silica interact abiotically to form iron silicates, providing an alternative iron formation deposition potentially independent of biologically-mediated processes (Rasmussen et al. 2021).

Previous studies evaluating mineralogy in silica-cemented horizons have generally focused on >2.5 Ga, pre-GOE iron formation (Beukes 1980, Rasmussen et al. 2014, 2015, 2017; Sheppard et al. 2017; Lantink et al. 2018; Tosca et al. 2019; Muhling and Rasmussen 2020), while fewer studies focus on the identification of mineral relationships in silica-cemented layers of Paleoproterozoic iron formations deposited following the GOE (Figure 1A-B). Intriguingly, multiple mineralogical studies of post-GOE iron formation note texturally early greenalite (French 1968, 1973; Floran and Papike 1975, 1978; Simonson 1987), and the presence of fine-grained Fe-Al-silicates (Rasmussen and Muhling 2020; Wacey et al. 2021). However, few studies have conducted in-depth examinations of iron silicate minerals in silica-cemented horizons in post-GOE iron formations (Rasmussen and Muhling 2020). Mineralogical studies of post-GOE iron formation are especially critical because the initial rise in oxygen may have been followed by decreasing oxygen in the Paleoproterozoic (Figure 1B; Planavsky et al. 2012; Kipp et al. 2017), which would impact the development and evolution of multi-cellular life. Additionally, careful mineralogical studies–when performed within a well-defined sedimentological and stratigraphic framework–may illuminate whether early oxygenation occurred in only shallow water or extended into deeper water during the mid-Proterozoic (Figure 1C), a long-studied and debated topic. Deciphering the origin and evolution of complex mixed valence iron silicate minerals may help to better constrain the persistence of reduced iron in deep water, which in turn links directly to the location of the oxygen boundary in the post-GOE water column.

Focusing on silica-cemented intervals as preservation windows into early forming mineral phases in the ocean after the rise in atmospheric oxygen, we observed the textural relationships and measured the chemical compositions of several different iron mineral phases in the post-GOE, ~1.9 Ga Biwabik Iron Formation. We applied a complimentary suite of methods to observe these iron minerals, including detailed petrography, scanning electron microscope (SEM) equipped with energy dispersive X-ray spectroscopy (EDS), electron probe microanalysis (EPMA) equipped with wavelength-dispersive spectroscopy (WDS), and Raman Spectroscopy. Pairing textural relationships with mineral compositional data, we identified unit-specific paragenetic sequences with texturally early iron silicates and associated diagenetic mineral transformations. The goals of the present study include: (1) to assess preservation potential of minerals within silica-cemented horizons of the Biwabik Iron Formation, (2) identify and analyze iron silicate minerals, and determine their relationships to surrounding phases, and (3) determine diagenetic reactions involving iron silicates and other iron mineral phases. Reconstructing mineral formation histories helps establish paragenetic sequences and associated conditions of formation for each mineral set. Identifying the conditions of formation for the earliest forming minerals allows for potential redox interpretations at or near the sediment/water interface. Following such an approach, future studies evaluating Archean and Paleoproterozoic iron formations as paleoenvironmental archives can evaluate early mineral preservation in silicified horizons to reconstruct unit specific paragenetic sequences, which may help to resolve disparate interpretations of redox conditions after the initial rise in oxygen on Earth.

GEOLOGIC BACKGROUND

The ~1.9 Ga Biwabik Iron Formation of the Mesabi range is part of the Animikie Group, a Paleoproterozoic sedimentary sequence extending from central Minnesota to southeastern Ontario that includes the iron formation of the Cuyuna range to the south and the Gunflint Iron Formation to the north (Figure 2A, B). The Animikie Group is one of several Paleoproterozoic supracrustal chemical and clastic sedimentary successions deposited from ~2200 to ~1780 Ma in the present-day Lake Superior region (Ojakangas 2001). Deposition of Paleoproterozoic sedimentary sequences began as continental extension and ocean opening caused basins to develop and accumulate sediment unconformably on the southeastern margin of the Superior craton (Schulz and Cannon 2007). Following the end of Animikie Basin sedimentation near ~1780 Ma (Heaman and Easton 2005), the later intrusion of the mafic Duluth Complex at ~1100 Ma isolated the likely-continuous Mesabi and Gunflint ranges of the Animikie Group, separating the two ranges with ~100km of plutonic, volcanic, and sedimentary rocks of the Midcontinent Rift System (Ojakangas 2001; Jirsa et al. 2008; Figure 2A, B). Iron formation proximal to but not removed by the Duluth Complex intrusion experienced contact metamorphism, though most of the iron formation including the drill core sample locations remain sub-greenschist facies

(Figure 2A, French 1968; Frost et al. 2007). Today, the Mesabi and Gunflint ranges dip southeast at ~10-20 degrees (Ojakangas et al. 2011).

In Minnesota, the Animikie group consists of the Pokegama Formation, the Biwabik Iron Formation, and the Virginia Formation (Figure 2C). The lowermost stratigraphic member, the Pokegama Formation, is a <50-meter siliciclastic unit composed of quartzite, argillite, and siltstone (Figure 2C). Radiometric Rb/Sr and Pb/Pb age dating of underlying dike swarms and cross-cutting quartz veins constrains Pokegama Formation deposition between 2125 ± 45 Ma and 1930 ± 25 Ma, respectively (Southwick and Day 1983; Hemming et al. 1990). During this depositional interval, paleo-environment interpretations based on observed bimodal cross-bedding sedimentary structures suggest deposition to be a near shore, tidally influenced shallow marine setting (Ojakangas 1983). Overlying the Pokegama formation is the Biwabik Iron Formation, a <225 m-thick chemical sedimentary unit whose inferred age of deposition comes from a single ash bed in the correlative upper Gunflint Iron formation dated at 1878.3 ± 1.3 Ma (Fralick et al. 2002), paired with the observation of the ~1850 Ma Sudbury Impact unit in the uppermost sections of the drill cores. The Biwabik Iron Formation is predominantly composed of authigenic iron minerals and chert. A low ~1% average Al_2O_3 composition (Morey 1992), coupled with the lack of visible terrestrial material in most drill core samples and thin sections indicates chemical sedimentation of the Biwabik Iron Formation occurred in a sediment-starved marine setting (Ojakangas 2001). However, some fine-grained beds have upwards of ~5% Al_2O_3 content (Morey 1992), and may contain terrestrial-sourced material too small to identify petrographically. Several thin sub-member horizons including the Basal Red and the Intermediate Slate contain significant terrestrial sediment (Figure 2C). Based on the gradational nature of the contact, the Basal Red likely represents a conformable transition from siliciclastic sedimentation of the Pokegama to chemical sedimentation of the Biwabik (Severson et al. 2009). Finally, directly overlying the Biwabik is the Virginia Formation, a siliciclastic sedimentary sequence composed primarily of alternating greywackes, siltstones, and argillites. Alternating bimodal grain sizes between beds and upwards coarsening packages suggest the Virginia Formation was largely deposited as turbidite sequences (Lucente and Morey 1983). Rare ash beds provide age constraints for the Virginia Formation at 1832 ± 3 Ma (Addison et al. 2005). Overall, the three formations of the Animikie basin share similar lithologies and stratigraphic packaging patterns with other iron formation-containing late Paleoproterozoic regional sedimentary sequences (e.g., Akin et al. 2013; Eyster et al. 2021).

The Biwabik Iron Formation subdivides into four informal, texture-based members, known as the Lower Cherty, Lower Slaty, Upper Cherty, and Upper Slaty. The descriptors “cherty" and “slaty" are mining terms based on gross-scale architecture and correlation between mine sites (Wolff 1917) and do not refer to the overall composition, cleavage, or metamorphic grade (Ojakangas 2011). Within cherty members, alternating >1-5 cm beds of silica-cemented (Figure 3A, B) and non-silica-cemented granules make up the primary sedimentary texture (Severson et al. 2009). Granules are typically sand-sized and resemble arenitic textures in siliciclastic sedimentary rocks (Simonson 1987). In the Upper and Lower Slaty members, beds are typically thinner (<1cm) and composed of silt to clay-sized material instead of granules (Figure 3C, D). However, rare beds composed of silt to clay-sized material and lacking silica cement can contain granules. In this study, samples that possess quartz, chert, or chalcedony cement will be referred to as “silica-cemented horizons" and layers that lack silica cement and contain a predominant (but not exclusive) grain size of silt and/or clay will be termed “banded horizons.” Both silica-cemented horizons and banded horizons can contain granules within this nomenclature; however, silica-cemented horizons always contain granules, whereas banded horizons more commonly lack granules, and are defined by a lack of silica cement. Throughout Biwabik stratigraphy, silica-cemented horizons appear as either (1) continuous ~5mm - 1 cm tabular beds, or (2) as ovoid nodules where laminae above and below deform around the nodule indicating formation pre-compaction (Figure 3A-D).

METHODS

Sample Selection

Representative samples from each Biwabik Iron Formation member were collected from drill cores LWD-99-01 and LWD-99-02 at the Department of Natural Resources Drill Core Library in Hibbing, Minnesota. Drill cores LWD-99-01 and LWD-99-02 were selected as they represent the thickest part of the Biwabik Iron Formation and contain abundant material from all four members (Figure 2B, C; Severson et al. 2009). Sixty-eight samples were selected from both drill cores spanning Biwabik Iron Formation stratigraphy as well as portions of the underlying Pokegama and the overlying Virginia Formation (Figure 2C, gray circles). Finding and collecting silica-cemented samples involved searching for gray-to white-colored silica-cemented features in drill core, primarily in the form of nodules or tabular horizons (e.g., Figure 3A-D). To compare mineralogy between different horizons, all 68 samples were made into polished thin sections, with subsets specifically focused on encompassing both silica-cemented and banded horizons in single thin sections for data comparison.

Optical Microscopy

Mineral identification was conducted using a Nikon SMZ1270/800N large-field stereoscope and a Nikon Eclipse LV100N POL transmitted light (TL) microscope equipped with reflected light capabilities. Mineral phases were initially identified using respective diagnostic features in plane polarized (PPL) and cross-polarized light (XPL), with reflected light used for identifying mineral phases that appear opaque in transmitted light including Fe-oxides and sulfides. In addition to initial mineral identification, the following textural data was collected: (1) cross-cutting relationships between mineral phases and granule/cement contacts (Tables 1, 2); (2) granular textures including shape and internal granule structures (Supplementary Table S1).

Scanning Electron Microscopy

Following detailed petrographic characterization, a subset of samples were imaged and analyzed using Scanning Electron Microscopy to: (1) observe textural relationships between mineral phases at higher resolution, (2) establish/ test cross-cutting relationships identified using petrography, and (3) confirm identification of silicate mineral phases. Backscattered electron (BSE) images were collected with a JEOL JSM-6490LV SEM instrument equipped with an Energy Dispersive Spectroscopy (EDS) detector at the University of Minnesota Duluth Research Instrumentation Laboratory. Before SEM analysis, thin sections were coated with ~15 ±5 nm of carbon using a LADD Vacuum Evaporator. Qualitative chemical compositions of mineral phases were measured with the EDS detector. Beam width for spot analyses varied between sessions but were typically ~5-100 μm wide to avoid analyzing multiple mineral phases per analysis. Spot analyses were operated at 10-15 kV with a ~70 second dwell-time. For select fine-grained samples, EDS element maps were collected to display distributions of Fe, Al, Mg, and Si in minerals too small for both EDS and WDS spot analyses (i.e., < than 3 μm). Element maps were collected across a ~200 by 200 μm area at 15 kV, with a map dwell time of 100 μs and a total run time of 92 minutes. Element maps of Fe and Si were edited into a composite element map using ImageJ software (Schneider et al. 2012).

Electron Probe Microanalysis

After mineral phases were identified via optical microscopy and EDS, fourteen samples were selected for quantitative mineral analysis by EPMA (Table 1). Minerals analyzed come from samples that span all four members of the Biwabik and include iron silicates and carbonates both inside and outside of granules, as well as from non-granular textures (Table 1). This EPMA data was collected using a CAMECA SXFive field emission (SN944) electron microprobe located at the University of Wisconsin-Madison. Element concentrations were measured for specific mineral phases using a WDS detectors for X-rays generated from spot analysis. Elements for iron silicates were measured with the following mineral standards: Na and Al in jadeite, Mg, Al, Si, and Ca in hornblende, K in K-feldspar, Fe in hematite, Mn in Mn-olivine, and O in clinochlore. For measuring elements in carbonates, the following standards were used: Ca and Mg in dolomite, Fe in siderite, and Mn in rhodochrosite. Notably, O was measured in silicates, but not in carbonates. Spot analyses were conducted at 15kV using a 20 nA electron beam current. The X-rays were recorded for 10 s on the characteristic X-Ray peak and for 5 s on the backgrounds on each side of the peak. Spot size was adjusted, from 3 to 20 μm, to prevent beam damage of the analyzed material, especially for carbonates, and to prevent additional mineral phases from being measured during spot analyses, with beam width smaller than the mineral being analyzed. Minerals with sub-μm crystals were also measured when they occurred in monomineralic aggregates >3 μm, such as in greenalite or chamosite-bearing granules.

Verification of whether two different mineral varieties were measured in a single analysis included checking for visual differences in BSE imaging and for variability in chemical composition totals between different spot analyses in the same sample. Both of these measurement types found minimal examples of two or more different sub-µm mineral phases. Chemical compositions from WDS spot analyses were measured, matrix corrected using the PAP φ(ρz) correction (Pouchou and Pichoir 1991) and the MAC30 mass absorption coefficients (Heinrich 1987) as implemented in the Probe for EPMA software (Donovan et al. 2021), and reported as weight percent (wt%) oxide totals (Table 3). Data containing error range for WDS point analyses and point analysis locations can be found in the Supplementary Table S2. A cut-off of <97-101 wt% total was used when selecting spot analyses for calculating carbonate, minnesotaite, and stilpnomelane mineral formulas. Spot analyses with wt% oxide totals from 95-101% were used when calculating greenalite and chamosite mineral formulas. Lower oxide totals were used for greenalite and chamosite mineral formulas since these phases had lower average totals as they are hydrated phases. The lower totals were likely caused by the sub-µm mineral habits and difficulty measuring water (in the form of OH). Cation totals from mineral formulas were then plotted on ternary diagrams (Klein 2005) to compare mineral compositions from this study with the minerals in other iron formations or Fe-rich sedimentary rocks.

Raman Spectroscopy and Hyperspectral Maps

Raman spectra were acquired on ~1 µm target spots using a Horiba XploRA PLUS Raman spectrometer coupled to an Olympus BX41 microscope. We used a 532 nm laser excitation source (~1 mW), focused through a 100X objective lens with a grating of 1200 lines/mm (750 nm) and a 100 µm confocal pinhole to optimize spatial and spectral resolution.

The spectrometer was calibrated prior to analysis using a Si reference (peak at 520 cm^{-1}) and spectra were collected on a TE deep-air cooled -60 ºC CCD detector. We corrected spectral data for instrumental artifacts and subtracted baselines when needed using a polynomial fitting algorithm in the Horiba LabSpec 6 software. We also applied a smoothing function to produce an average of 5-10 adjacent points to remove background noise.

Hyperspectral maps of target areas were additionally produced to reveal complex mineral interactions observed in the samples. We produced these maps by rastering the microscope stage across a target region to generate spectra at each pixel. The hyperspectral dataset was fit by finding spectral endmembers within the map and applying a multicomponent Classical Least Squares fitting of endmembers to each pixel within the LabSpec 6 software. This quantitative analysis yielded a 'score' that we used to produce a color map showing the dominant phase at each pixel. Each endmember was matched to a known standard, either from internal lab collection or using the RRUFF public Raman database (Lafuente et al. 2015).

RESULTS

Within the Biwabik Iron Formation, the following minerals were identified via optical microscopy, SEM with EDS, EPMA with WDS, and Raman Spectroscopy: quartz, iron silicates (greenalite, chamosite, minnesotaite, stilpnomelane), carbonates (siderite, ankerite-dolomite, calcite) and iron oxides (hematite, magnetite). Results will be presented in two sections divided into focusing on the iron silicate mineralogy and then briefly describing the carbonate and iron oxide mineralogy. Textural attributes such as grain shape, morphology and internal textures were found to be closely related to specific mineral phases and are discussed in each respective mineral section. Textural and mineral data is reported in Tables 1-3 and Supplementary Table S1. Mineral formulae are reported in Table 3 and Supplementary Table S2.

Iron silicate mineralogy

Chamosite. Chamosite, an Fe-rich chlorite [$(Fe,Al)_6(Si,Al)_4O_{10}(OH)_8$], occurs in granules as aggregates of sub-μm crystals. Chamosite mineral composition was measured from granules in three samples, MIR-19-12, MIR-19-15, and MIR-17-18 (Figure 4A, square symbols). Granules in MIR-19-12 and MIR-19-15 were located in and near banded horizons and in adjacent silica-cemented horizons (Figure 5A, sample MIR-19-12; Figure 5B -C, sample MIR-19-15), while chamosite mineral compositions in MIR-17-18 were collected within a banded horizon. Chamosite mineral data from all three samples range from 31-40 wt% FeO, 24-30 wt% SiO_2, 2-17 wt% Al_2O_3, and 6-14 wt% MgO (Figure 4A, Table 3, and Supplementary Table S2). No discernible differences in composition are noted between chamosite granules within the same sample. Chamosite contains significantly more Al_2O_3 relative to greenalite, minnesotaite, and stilpnomelane from this study (Table 3 and Supplementary Table S2).

Chamosite-bearing granules are mostly distributed within banded horizons or in silica-cemented horizons adjacent to banded horizons (Figure 5A-C). An example of this distribution can be seen in Figure 5A, where chamosite granules occur along the margins of a chert nodule (zone 1; Figure 5A) but decrease in density from the center of the nodule (zone 2, Figure 5A). In zone 2, chamosite is present as finely disseminated crystals, but granules are predominately composed of microcrystalline quartz. No chamosite was identified outside of granule boundaries as cement, although very fine-grained (<1 μm) chamosite is present in banded horizons (zone 3, Figure 5A, B). Texturally, chamosite is sometimes crosscut by stilpnomelane (Figure 5D), carbonates, hematite, and/or magnetite. Notably, chamosite was not observed alongside greenalite within the same local mesobands or horizons.

Stilpnomelane. The Fe-silicate stilpnomelane [$(Fe,Mg,Al)_{2.7}(Si,Al)_4(O,OH)_{12} \cdot nH_2O$ with traces of K, Na, Ca; Klein 2005] forms ~3 -100 µm long subhedral-euhedral acicular or bladed crystals (Figure 5D). Stilpnomelane mineral compositions were measured from two banded horizon samples (MIR-19-3.5 and MIR-U-08; Figure 4B) and one silica-cemented sample (MIR-17-16; Figure 4B). Mineral compositions for stilpnomelane in sample MIR-17-16 were measured from crystals within a chert intraclast with no adjacent banded horizon (Duncanson 2020). All three stilpnomelane samples possess relatively comparable values of 43-49 wt% SiO_2, 3- 5 wt% Al_2O_3, and low but appreciable levels of 1- 2 wt% K_2O and ~0.5 wt% Na_2O (Table 1; Supplementary Table S2). Stilpnomelane from banded-horizons (MIR-19-3.5 and MIR-U-08; Figure 4B) contained lower Fe and higher Mg contents (25- 26 wt% FeO, 11-13 wt% MgO; Figure 4B, dark green/red diamond symbols) compared to stilpnomelane from silica-cemented horizons (34 wt% FeO, 3 wt% MgO; Figure 4B, light green diamond symbols). Stilpnomelane composition from the present study overlap with respect to Fe-Mg-Al concentrations measured in stilpnomelane from other iron formations (Figure 4A, B shaded gray region; Gole 1980 and Klein 2005).

Texturally, stilpnomelane distribution is highest within banded horizons, though it occurs as an internal granule phase as well as an intergranular cement among silica-cemented horizons as well. Stilpnomelane crystals commonly crosscut chamosite (Figure 5D) and greenalite. Stilpnomelane is always crosscut by magnetite and coarse ≥5 µm hematite crystals when these minerals are present, and sometimes crosscut by large, euhedral carbonate crystals.

Minnesotaite. The Fe-rich talc endmember minnesotaite [$Fe_3Si_4O_{10}(OH)_2$] most commonly forms bundles of ~5-50 μm long subhedral-euhedral acicular crystals resembling "felty masses" (Floran and Papike 1975). Minnesotaite mineral compositions were collected from intergranular and interstitial crystals in six samples (MIR-19-3.5, MIR-U-08, MIR-19-05, MIR-L-07, MIR-U-10, MIR-17-13; Figure 4C). Point analyses were collected for individual minnesotaite crystals or from homogenous minnesotaite crystal masses (Figure 6 A-F, Figure 7A-H). Raman spectroscopy analyses on three samples (MIR-L-07, MIR-U-10, MIR-17-13) additionally confirmed the identification of minnesotaite (Figure 7H).

Texturally, minnesotaite crystals crosscut sedimentary textures including granule-cement boundaries and non-compaction fractures within chert and greenalite granules (Figure 6A-D; Figure 7C-G). Minnesotaite commonly crosscuts greenalite and/or occurs as a first-generation cement phase associated with greenalite granules (Figure 6B, Figure 7D, G). In addition to occurring in direct association with greenalite, minnesotaite is also present as the only internal phases in some granules (Figure 6C, D). In these instances, minnesotaite occurs internal in the granule, and as a first-generation cement (Figure 6D). In two samples (MIR-19-3.5 and MIR-U-08) both stilpnomelane and minnesotaite mineral compositions were measured (Figure 4B, C). In sample MIR-19-3.5 (Figure 6E-G), minnesotaite granules are preserved inside the silica-cemented horizon (Figure 6E, F) and stilpnomelane granules are preserved at the margin of the silica-cemented horizon (Figure 6E, G). In this sample, stilpnomelane crosscuts minnesotaite (Figure 6G), but generally throughout the section, minnesotaite alternates cross-cutting relationships with both stilpnomelane and carbonate crystals indicating multiple generations of regrowth and/or recrystallization of those phases. Minnesotaite is always crosscut by euhedral magnetite when present (Figure 6F, G).

Minnesotaite mineral compositions (Figure 4C) in samples MIR-L-07 (Figure 6A, B; Figure 7F,G), MIR-U-10 (Figure 7A-E), and MIR-17-13 (Figure 8A-F) come from silica-cemented horizons and show a direct textural relationship with greenalite (e.g., Figure 6B), while minnesotaite in samples MIR-19-05 (Figure 6C-D), MIR-U-08, and MIR-19-3.5 (Figure 6E-G) were measured from silica-cemented horizons that lack greenalite (Figure 6C-G). Minnesotaite bundles that occur within granules compared to those that occur as interstitial cements show no difference in composition in the same sample. However, a large compositional difference was measured for FeO and MgO content between minnesotaite texturally associated with greenalite (e.g. sample MIR-L-07; Figure 4C) compared to minnesotaite associated with stilpnomelane (e.g. sample MIR-19-3.5; Figure 4C). Minnesotaite in stilpnomelane-rich samples MIR-19-3.5 (Figure 6E and F) and MIR-U-08 have similar ~17 wt% FeO and ~20 wt% MgO compositions (Figure 4C; Table 3, Supplementary Table S2), whereas minnesotaite from greenalite-bearing samples MIR-L-07, MIR-U-10, MIR-19-05, and MIR-17-13 have higher average 33-42 wt% FeO and lower 2-7 wt% MgO (Figure 4C). Additionally, Raman point spectra confirm the presence of minnesotaite in these samples despite its FeO content measuring higher than expected. Consequently, the MgO and FeO content of stilpnomelane-associated minnesotaite (Figure 6E and F) resembles the talc-minnesotaite series compositions observed in other iron formations (Klein 2005), whereas minnesotaite alongside greenalite and/or lacking stilpnomelane contain enough FeO to plot outside of Klein (2005) mineral series (Figure 4C). Similar Fe-rich minnesotaite is noted in the Gunflint Iron Formation (Floran and Papike 1975).

Greenalite. Greenalite was identified in several Biwabik samples through a combination of mineral composition and Raman spectroscopy. Greenalite, the iron endmember mineral from the serpentine clay group [ideal formula: $Fe_3Si_2O_5(OH)_4$)], is present among silica-cemented horizons in two distinct habits: (1) as aggregates of sub-µm crystals which constitute whole granules (Figure 7A-G), resembling greenalite granules previously noted in the Biwabik and Gunflint Iron Formation (Leith 1903; French 1968, 1973; Floran and Papike 1975); and (2) as sub-µm disseminated inclusions within chert granules giving an overall 'dusty' appearance (Figure 8G-I), similar to greenalite-bearing chert in banded iron formations (Rasmussen et al. 2017; Muhling and Rasmussen, 2020). As previously described, some granules contain a mixture of fine-grained, disseminated greenalite and minnesotaite (Figure 8A, B) where minnesotaite occurs inside granules (Figure 6F, 8F) and as an intergranular, first-generation cement (Figure 8C). Other samples contain granules composed entirely of greenalite, and minnesotaite only occurs as intergranular cement nucleating off the exterior boundaries of granules (Figure 8D – F) or nucleating from granules into quartz-filled non-compaction fractures (ncf) inside individual granules (Figure 7G). Non-compaction fractures (ncf; Figure 7F, G) are common in greenalite and chert granules throughout the drill core. Notably, greenalite is only found within granules and not as an intergranular cement phase among the surrounding quartz cement. Aggregates of greenalite appear dark green to opaque in transmitted light. Both the disseminated and aggregate forms of greenalite were only found within silica-cemented horizons, and were not identified within banded horizons, though the possibility exists of unidentified fine-grained (sub-µm) greenalite disseminated within banded horizons.

Mineral composition data (Figure 4D; 7H) was collected from two samples (MIR-U-10; Figure 7A - F; MIR-L-07; Figure 7G, H) containing granules with aggregates of sub-µm crystals large enough (> 3µm) for microprobe point analysis. Samples MIR-L-07 and MIR-U-10 range in composition from ~45-51 wt% FeO, 33-34 wt% SiO_2, and contain appreciable ~3-6 wt% MgO content (Figure 4D; Table 3, Supplementary Table S2). Minnesotaite cement was also measured from three samples containing greenalite granules (Figure 4C, and Figure 7E, H). The chemical compositions of greenalite in both samples resemble greenalite in other iron formations (Figure 4D, greenalite field); this includes a minor excess of Si relative to the ideal 4.00 Si in greenalite, with an average 4.13 and 4.05 Si formula ions in MIR-L07 and MIR-U-10. respectively (Table 3 and Supplementary Table S2). Excess Si ions are noted for microprobe measurements of greenalite in other iron formations, likely linked to sub-μm quartz impurities present within aggregates of greenalite (Floran and Papike 1975; Gole 1980). In some instances, there appeared to be a mixture of two phases present near noncompaction fractures inside granules (Figure 7E), which could be due to sub-μm quartz impurities and/or excess Si (Gole 1980). Disseminated greenalite inclusions within chert granules were too small (< 1 μm) for WDS spot analysis and were instead measured semi-quantitatively with EDS spectra (Figure 8G-I). Based on their high Fe, Si, and O peaks, with smaller Mg peaks, these inclusions were identified as greenalite, similar to other iron formation studies (Figure 8G-I; Muhling and Rasmussen 2020).

Carbonate and iron oxide mineralogy

Carbonate minerals are most commonly present as large (~0.1 - 5mm) subhedral-euhedral crystals (Figure 9A, B). Texturally, large carbonate crystals occur in the highest density within banded horizons and directly adjacent to banded horizons. Within silica-cemented horizons, carbonates typically transect granule-cement contacts (e.g., Figure 9A) and crosscut most iron silicate minerals, although because there are multiple generations of carbonate crystals, this phase can show both earlier and later cross-cutting relationships with minnesotaite and stilpnomelane crystals (Figure 9B). In addition to occurring proximal to or as banded layers

(Figure 7A, bands), carbonate crystals also appear in chert intraclasts (Figure 9C, D). Compositionally, carbonate crystals typically have varying FeO, MgO, and CaO content resulting in an array of ferroan dolomite-ankerite series to siderite compositions (Figure S1). This compositional variation is noted between the rims and cores of single crystals as well as between carbonate minerals from different samples and is typical of ferroan dolomite-ankerite series carbonates within other iron formations (Krapež et al 2003; Flügel and Munnecke, 2010). Carbonate crystals are consistently crosscut by magnetite (Figure 9E) and coarse hematite crystals (Figure 9F, G). Preliminary results of Biwabik carbonate textures and additional context for compositional data are presented in the M.S. thesis by S. Duncanson (Duncanson, 2020) and are the subject of a separate study.

Magnetite and hematite are the most common iron oxides observed throughout the Biwabik Iron Formation. Magnetite (Fe_3O_4) forms ~10-20 μm euhedral crystals (Figure 9E-G). It crosscuts all other minerals phases when present, including coarse hematite (Figure 9F, G). Hematite (Fe_2O_3) crystals range from fine grained (<1-5 μm; Figure 9H) to coarse ($\geq$5 μm) euhedral laths (Figure 9E-G). Both fine- and coarse-crystal sizes are found within chert granules, as cement in both silica cemented and banded horizons as well as uniquely forming concentric layers of chert-hematite ooids in the Basal Red and Upper Cherty units (Figure 2), as well as in stromatolitic horizons of the Lower Cherty (Planavsky et al. 2009; Severson et al. 2009). Coarser crystal hematite laths most typically crosscut Fe-silicate and carbonate minerals, granule-cement boundaries, and quartz cement between granules (Figure 9F, G). Fine, nanoscale hematite constitutes layers which coat grains (Figure 9H). Importantly, such examples of fine-grained hematite are not seen alongside greenalite and minnesotaite, and instead are present in samples with abundant microquartz (Figure 9H). Therefore, although there may be other stratigraphic intervals where iron oxides are primary, hematite mineralizing within the examined Fe-silicate-rich samples all appears secondary.

DISCUSSION

In the following discussion, we suggest interpretations of primary and secondary relationships of iron minerals, propose iron silicate diagenetic reactions using mineral compositions and textural relationships, and then develop a paragenetic sequence model based on textural observations in the Biwabik Iron Formation. Below, we describe cross-cutting relationships and compositional data for diagenetic and texturally early minerals observed in silica-cemented horizons and compare these features to adjacent banded horizons to inform potential mineral reactions and identify possible precursor mineral phases. We define texturally early minerals following a modified version of the “primary mineral” classification for iron formation mineralogy described in Laberge (1964), including (1) a very fine grain size (combined with the information that samples only experienced low temperature and pressure conditions throughout their history, indicating that grain size reduction during metamorphism is unlikely); (2) a uniform size distribution; (3) a particulate or granular texture, and (4) a close association with sedimentary features such as bedding. In the present study, minerals that meet all four Laberge (1964) criteria are termed ‘texturally early’ to recognize that they may still form after other minerals. We also acknowledge that geochemical exchange may have occurred during the transformation from amorphous phases to crystalline minerals. Furthermore, we observed that some fine-grained minerals cross-cut other minerals and thus likely form a sequence of identifiable mineral reactions that occurred during early diagenesis. In addition, we add the criteria that texturally early minerals should occur within early chert granules and do not transect granule-cement contacts or occur as intergranular cements. Minerals formed outside of granules but within the same horizon are interpreted based on their textual relationship to granules, and as a result, are identified as occurring after granule formation.

The focus of the present study is the documentation of mineral relationships, specifically those preserved in silicified horizons of the Biwabik Iron Formation. The discussion centers on interpretations of observed textures and compositions in such horizons. In the following section, we outline diagenetic mineral relationships preserved in silicified regions of the Biwabik Iron Formation, following our mineralogical identifications and interpretations by interpretations of texturally early phases, with a focus on deciphering the origin of iron silicate phases preserved in the Biwabik Iron Formation.

Texturally early minerals in the Biwabik Iron Formation

Textural relationships between mineral phases within silica-cemented horizons preserve clear evidence of their relative timing of precipitation, providing insights into possible precursor sediment composition(s). Through the previously described framework, we identified texturally early minerals of the Biwabik Iron Formation to include microcrystalline quartz (in the form of chert), greenalite, and chamosite, and fine-grained hematite. Minerals identified as having a clear secondary, diagenetic origin include stilpnomelane, minnesotaite, euhedral carbonate crystals, and magnetite. Some fine-grained hematite examples show evidence for texturally early formation (Figure 9H), though most commonly, these phases occur as clear diagenetic minerals that cross-cut earlier phases (e.g., Figure 9A, F, G). Examples of texturally early fine-grained hematite include crystals that are distributed as sub-μm crystals within stromatolite layers or coated chert grains in restricted horizons (e.g., Basal Red unit, Figure 2; Figure 9H).

Microcrystalline quartz is a pervasive early cement in silicified horizons, commonly crosscut by later minnesotaite and stilpnomelane cement, as well as euhedral carbonate and magnetite. The formation of chert nodules surrounded by differentially compacted banded layers (e.g., Fig. 3D) supports microcrystalline quartz being an early phase in the Biwabik Iron Formation sediments. Chert granules commonly show non-compaction fractures (e.g., 8G, H) interpreted as dewatering fractures linked to dehydration of an initial hydrous silica-gel granule composition (Simonson 1987; Maliva et al., 2005). Initial hydrous silica may have been deposited via adsorption onto settling precursor sediment (Fisher and Knoll 2009; Konhauser et al. 2017; Rasmussen and Muhling 2020) and/or as a primary SiO_2 precipitate (Stefurak et al. 2014; 2015).

Greenalite does not cross-cut other mineral phases from this study, and is not observed filling non-compaction fractures, or as a cement phase, suggesting greenalite precipitation occurred prior to granule fracturing. Granules composed primarily of greenalite display dewatering fractures filled entirely with quartz cement (Figure 7B; 8G), suggesting greenalite precipitation concurrent with or prior to dewatering. If greenalite formation occurred after dewatering, then we would expect fractures to be filled with or crosscut by greenalite, similar to the minnesotaite that nucleates off granule surfaces into non-compaction fractures or surrounding granules as a first-generation cement in these samples (Figure 7G; 8C). Pairing these textural observations with greenalite mineral composition supports interpretations of iron silicates as texturally early phases.

Both greenalite within chert granules and greenalite aggregates from the Biwabik Iron Formation share similar compositional ranges (Figure 4D) and textural habits with greenalite from other iron formations (Floran and Papike 1975; Rasmussen et al. 2017, 2019; Johnson et al.

2018; Muhling and Rasmussen 2020). These prior studies suggest that greenalite compositions most closely approximate the initial primary precipitate composition based on textural observations. For example, dusty chert beds containing silica-cemented greenalite inclusions in late Archean and early Proterozoic iron formation are interpreted to represent the precursor sediment consisting of greenalite or a greenalite-like precursor phase (Muhling and Rasmussen 2020). Sub-μm greenalite in dusty chert granules of the Biwabik Iron Formation visually resemble dusty chert beds as well as resembling “cloudy” chert granules containing a sub-μm silicate phase in other late Paleoproterozoic granular iron formations (Simonson 1987). If greenalite in the Biwabik Iron Formation closely approximates the precursor sediment composition, then granules likely have a precursor composition with significant ferrous iron, silica, and water, resembling a greenalite-like gel (Tosca et al. 2016, 2019; Hinz et al. 2021). Alternatively, texturally early greenalite could mineralize after reduction of a precursor iron (oxy)-hydroxide or similar phase (Robbins et al. 2019), though no direct textural relationships were observed in samples to support or identify such reactions.

Fine-grained chamosite provides insight into precursor sediment composition as well, though the distribution of chamosite granules within silica cement and its high aluminum content suggest its likely precipitation during early diagenesis at the same time as or shortly after the precipitation of chert and potentially other iron-bearing primary mineral phase(s). Unlike greenalite, chamosite does not form ubiquitously within silica-cemented horizons, but instead forms adjacent to or within banded horizons (Figure 5A-C). The limited spatial distribution of chamosite granules is likely due to the high aluminum content of chamosite, with sufficient aluminum most likely sourced from fine-grained terrestrial or volcanic-derived material within banded horizons (Morey 1992). Due to the limited mobility of aluminum in pore fluids (Wintsch and Kvale 1994), chamosite could be restricted to forming proximal to aluminum sources in the banded horizons, while silica and iron could derive from a precursor sediment phase within granules. An example of aluminum-dependent distribution can be seen in Figure 5A (zone 1) where green-colored chamosite granules are more abundant close to the banded horizon along the margins of the nodule while the center of the nodule contains light-toned granules composed primarily of chert (Figure 5A; zone 2).

Since chamosite is still fine-grained and crosscut by diagenetic mineral phases such as euhedral carbonate, we propose that the likely precursor phase for chamosite in the Biwabik was a hydrous iron-silica gel that reacted with local aluminum-bearing sediments, similar to the mechanism proposed by French (1973). Local aluminum, silica, and iron-rich precursor phases are suggested for chamosite formation in other iron-rich rocks (Klein 2005). Specific examples of local aluminum influence on chamosite formation include chamosite-bearing ooids in Ordovician ironstones, where sufficient silica, iron, and aluminum concentrations for chamosite precipitation were supplied by rapidly deteriorating volcanic ash (Sturesson et al. 2000) and chamosite wisps in the Gunflint Iron Formation, where chamosite is restricted to tuffaceous shale facies and interpreted to form from precursor volcanic shards (Floran and Papike 1975). Formation of chamosite from an amorphous iron hydroxide-silica precipitate in the presence of iron, aluminum, and magnesium can occur under low temperature reducing conditions (Harder 1978).

We recognized two types of hematite which we distinguished as early and secondary. Most typically, hematite forms >5 μm euhedral to subhedral crystals which transect granule-cement contacts, indicating formation following granule deposition and silica cementation (Figure 9F, G). Therefore, these large hematite crystals which crosscut texturally early minerals in the Biwabik Iron Formation or form outside of granules in association with cement are classified as secondary. In contrast, we observed in the Basal Red and Upper Cherty stratigraphic intervals (Figure 2C) examples of sub-μm scale hematite within layers coating grains, which were labeled as texturally early. Other examples of fine-grained hematite in the Gunflint and other iron formations have been found to cross-cut Fe-silicates, suggesting the phase may form secondarily while remaining fine-grained (Rasmussen et al. 2016; Rasmussen and Muhling 2020). Additionally, because the water column was likely stratified with respect to oxygen and iron concentrations across the Proterozoic, it is possible and very likely that shallow water and deeper water units possess different sets of texturally early phases that relate back to the position of the oxygenated boundary in the water column (commonly called the redoxcline). As a result of this chemistry, in the oxygenated part of the water column, hematite may form as an early mineral phase from oxidized waters, which may explain why observations of fine-grained hematite in the Biwabik Iron Formation are limited to stromatolitic horizons, coated grains, or associated thin laminae.

Secondary iron silicate mineral compositions

In addition to preserving texturally early greenalite and chamosite, silica-cemented horizons also preserve minnesotaite and stilpnomelane assemblages that crosscut texturally early phases and granule-cement boundaries. Euhedral to subhedral acicular minnesotaite and stilpnomelane crystals (~50 μm or less) visibly cross-cut granule-cement boundaries and appear as interstitial cement phases, and often cross-cut chamosite (Figure 5D) and greenalite (Figure 6B; 7G). Such textural relationships suggest minnesotaite and stilpnomelane form after granule formation and both during and/or after silica cementation. However, the presence of stilpnomelane inclusions within pebble-size chert intraclasts (Figure 9C, D) and not in the surrounding granules or cement suggests stilpnomelane can form prior to erosion, transportation, and redeposition of intrabasinal chert intraclasts. Transport and redeposition of stilpnomelane-bearing chert intraclasts suggest stilpnomelane may be able to form close to the sediment-water interface (Simonson 1987). This interpretation is in line with previous studies, where acicular stilpnomelane and minnesotaite were classified as forming during early diagenesis in granular iron formation (Dimroth and Chauvel 1973; Floran and Papike 1975) and banded iron formation (Gole 1980; Pecoits et al. 2009). Minnesotaite and stilpnomelane likely form from secondary reactions of texturally earlier iron silicates.

Minnesotaite is commonly observed cross-cutting greenalite granules and/or as a cement (Figure 6D; Figure 8C-D) and likely forms as a reaction product of greenalite and chert (French 1973; Klein 2005). Compositionally, minnesotaite that crosscuts greenalite or forms cement between greenalite granules is Fe-rich, resembling greenalite compositions within the same sample (Figure 4C, D). We hypothesize that samples lacking greenalite but containing granules that are predominantly composed of Fe-rich minnesotaite (Figure 4C; Figure 8A-C) may derive from complete replacement of greenalite in diagenetic environment with abundant silica. This mechanism is supported by our observations of granules in sample MIR-17-13 where Raman spectroscopy showed greenalite-dominated granules with varying admixtures of minnesotaite within the granules and minnesotaite-dominant cross-cutting cement and small veinlets (Figure 8D-F). Alternatively, Fe-rich minnesotaite may originate from reactions with other iron bearing texturally early precursors such as hematite, siderite, or chamosite reacting with chert (Floran and Papike 1978). However, no clear examples of hematite or chamosite being crosscut by minnesotaite were observed in this study, whereas there were abundant observations of minnesotaite cross-cutting greenalite.

Assuming greenalite or similar iron and silica-bearing phases are precursors for Fe-rich minnesotaite, then minnesotaite with higher magnesium content may indicate a more Mg-rich precursor phase and/or magnesium incorporation (or Fe loss) during diagenesis. Unlike the iron-rich minnesotaite that is distributed solely within tabular silica-cemented horizons (Figure 6A), granules containing Mg-rich minnesotaite (MIR-U-08 and MIR-19-3.5, Figure 4C) are in silica-cemented nodules surrounded by fine-grained banded horizons (Figure 6E). Within these nodules, minnesotaite granules located adjacent to the nodule margins are crosscut by additional diagenetic mineral phases, including stilpnomelane (Figure 6G). These minnesotaite and stilpnomelane crystals have similar chemical compositions, containing significantly higher magnesium and lower iron concentrations than the same mineral phases in tabular silica-cemented horizons (Figure 4B, 4C). In these samples, Mg-rich minnesotaite is found near banded horizons and cross-cutting stilpnomelane, suggesting banded horizons and/or their precursory sediment-pore fluid admixture, could be a potential magnesium source (Gole, 1980). The higher abundance of cross-cutting diagenetic minerals like stilpnomelane along chert nodule margins (Figure 3B) suggests a greater degree of diagenetic mineralization, perhaps driven by additional exposure to diagenetic pore fluids within the surrounding banded horizon. Assuming Mg-rich minnesotaite granules have the same iron and silica precursor phases as the Fe-rich minnesotaite within tabular silica-cemented horizons, then diagenetic Mg-bearing pore fluids sourced from the banded horizons could have altered the original iron and silica precursor phases. Pore fluid interaction could have also driven a mineral reaction from minnesotaite to cross-cutting stilpnomelane with a similar iron and magnesium composition, albeit with an additional influx of aluminum. Stilpnomelane observations from the present study are in line with previous work on Gunflint and Biwabik Iron Formation mineralogy, which also suggest stilpnomelane can form from precursor minnesotaite (Floran and Papike 1975; McSwiggen and Morey 2008).

The observed distribution of stilpnomelane in samples MIR-U-08 and MIR-19-3.5 (Figure 5D; 6E, G) is common, where stilpnomelane typically crosscuts chamosite or minnesotaite near banded horizons. The textural association of chamosite and stilpnomelane near banded horizons (and significant concentrations of aluminum in both phases; Table 3, Figure 4A, B) may point to a local aluminum source from adjacent (non-silica-cemented) bands for both minerals. In addition, stilpnomelane contains significant magnesium, potassium, and sodium concentrations relative to the other iron silicates in this study (Table 3), suggesting diagenetic fluids capable of sourcing these elements likely played a key role in stilpnomelane formation as well (Gole 1980). We therefore propose that stilpnomelane likely forms from precursor phases in the Biwabik that can supply sufficient iron, aluminum, magnesium, and silica incorporating additional potassium and sodium from fine-grained material in surrounding banded horizons during mineralization. Previous Biwabik mineralogical studies proposing stilpnomelane precursors include chlorite and quartz (French 1968) as well as volcanic and/or extrabasinal siliciclastic material within banded horizons (French 1973). The source of aluminum for stilpnomelane-rich units within iron formation of the Transvaal Supergroup are also attributed to the input of volcanic material (Beukes and Klein 1990).

Reversing diagenetic reactions to identify primary precipitates that link to seawater

In both banded and silica-cemented horizons of the Biwabik Iron Formation, mineral assemblages preserve a sequence of incomplete diagenetic reactions which allow the development of paragenetic sequence sets. By pairing the relative order of formation between texturally early and secondary, diagenetic minerals with mineral compositions, we can identify the relative order of mineral precipitation and associated geochemical exchange. Reversing these geochemical reactions, we can potentially determine a set of potential precursor mineral compositions that may link back to seawater composition.

In this study, we found that horizons that lack silica cement show evidence for local geochemical exchange between pore fluids and hydrous iron and silica precursor sediments. Silicates adjacent to or among banded horizons incorporate more aluminum and/or magnesium (forming chamosite, stilpnomelane, and minnesotaite associated with stilpnomelane; Figure 4A-C). Silicates proximal to banded horizons are also crosscut by carbonate and iron oxide minerals more frequently than those within tabular silica-cemented horizons. In tabular silica-cemented horizons, the likely rapid encapsulation of precursor sediment immediately following deposition could reduce geochemical interaction with local terrestrially sourced sediment and/or oxidizing fluids to varying degrees.

Within tabular layers cemented by silica, we observe silicates with iron endmember compositions (Figure 4C, mns; Figure 4D, gre), and minerals that lack Al and Mg. This may be because silicified layers would have little to no interaction with diagenetic fluids and the surrounding sediment after cementation. Silicified layers may therefore present the best geochemical record of mineral interactions that occur at/ near the sediment-water interface. Using a holistic approach of putting together mineral compositions, cross-cutting relationships, and observed spatial distributions of phases within silica-cemented horizons, we interpret possible mineral reactions from the precursor sediment through diagenesis in silica-cemented and banded layers of iron formation and illustrate these with emphasis on iron silicates in Figure

10. We recognize the importance of oxide and carbonate phases in iron formation and their potential link to seawater conditions as primary minerals in some settings. In this work, the presence of texturally early oxides in some horizons of the Biwabik does not alter conclusions regarding the importance of early silicates for the Biwabik Iron Formation. Instead, it highlights the need for paired mineralogy and stratigraphy studies in order to detangle stratigraphic patterns in mineral distributions, which is the focus of ongoing work in the region.

The earliest forming minerals identified in the Biwabik Iron Formation are most commonly greenalite and chert within granular silica-cemented or banded horizons, and hematite, which is confined to stromatolitic or ooidal horizons. Importantly, in samples that meet the criteria to preserve texturally early phases, the two texturally early redox sensitive minerals (greenalite, hematite) are not found in association with one another, but instead are found in separate parts of the stratigraphy. The lack of a direct textural connection between the two texturally early phases could support the presence of an oxygen gradient or redoxcline within the basin (Akin et al. 2013) or may indicate the potential for partial oxidation of reduced phases within the water column or at/near the sediment-water interface. Because the Biwabik Iron Formation was deposited after the GOE and there is experimental support that mixed-valence proto iron silicate phases readily form (Hinz et al. 2021), we suggest the primary precipitates in the Biwabik Iron Formation were mixed Fe^{2+} and Fe^{3+} valence state, silica-rich gels ($Fe^{2+,3+}$-Si-O-OH) (Figure 10A).

We also identify that silicification (both nodular, and tabular) occurs very early, likely at the sediment water interface. To illustrate these two modes of silicification (nodular and tabular) and account for the differences we see in post-depositional mineral assemblages of silicified layers compared to non-silicified layers, we divide initial sediment deposition into three scenarios in Figure 10A. In scenario 1 (left panel of Figure 10A), there is little to no silica added to the initial sediment (non-silicified). In scenarios 2 and 3 (the middle and right panels of Figure 10A), silica is added to the sediment (as H_4SiO_4) and is likely sourced from seawater, as seawater silica concentrations were high across the Paleoproterozoic prior to the evolution of silica-secreting organisms (Siever 1992). Additionally, we account for potential addition of terrigenous material and its effects on the composition of some diagenetic minerals in scenarios 1 and 2 based on the data from the present study.

Post-deposition (Figure 10B), there are different mineral sets and unique textural relationships preserved between phases for each scenario. With limited silicification in scenario 1, primary precipitates are susceptible to post-depositional changes, which could include redox reactions. If oxygenated fluid interacts with the sediment at any point, then primary reduced or mixed phases will oxidize (Figure 10B, reaction pathway B1; reaction 1). This type of oxidation could occur, for example, during sea level fall and subsequent intersection of reduced sediments with the oxygen boundary in the water column (e.g., Todd et al. 2019), or through later fluid migration along bedding planes or fractures at any time in the geologic history of the unit (Losh and Rague 2018). With the lack of silica cement, reactive minerals are likely to exchange cations, resulting in the formation of phases like stilpnomelane (Figure 10B; reaction pathway B1; reaction 2). Even with limited cementation during formation of chert nodules (Figure 10B; scenario 2) fluid flow and geochemical exchange may occur at the boundaries of silicified areas and banded (non-silica-cemented) layers. Here, aluminum sourced from terrigenous material may promote local formation of both chamosite and stilpnomelane at or near nodule boundaries (Figure 5A-C; Figure 10B; reaction pathway B2; reaction 5,6). Based on our observations, we propose that a geochemical gradient preserves the inner chert nodules, where in the center (earliest precipitating) part of the chert nodule, granules composed of the precursor sediment mineralize to iron silicates and quartz (Figure 10B; reaction pathway B2). Only in scenario 3, where entire beds are silicified, do we see maximum preservation of reduced iron silicate phases such as greenalite (Figure 10B; reaction pathway B3; reactions 7, 8), along with a lack of textural and compositional evidence for local geochemical exchange. In all three scenarios, carbonate minerals, represented in Figure 10 as siderite, form after silicate minerals (Figure 10B, reactions 3, 9). Some carbonate crystals are observed forming prior to minnesotaite and stilpnomelane (Figure 5D, and Figure 9B), indicating some secondary iron silicates continue forming after carbonate formation, most carbonate minerals cross-cut silicate phases (Figure 9A). Magnetite crystals cross-cut carbonate and all other mineral phases (, Figure 6G; Figure 9E-F) and are the last forming mineral in all three scenarios (Figure 10B, reaction 4). The higher proportion of magnetite observed in banded horizons relative to silica-cemented ones further suggests increased local geochemical exchange between pore fluids and earlier forming reactive minerals, resulting in increased magnetite mineralization from precursor siderite (Figure 10B, reaction 4) and/or iron silicates (Figure 6D; Rasmussen and Muhling 2018). Overall, we therefore conclude that silicification links to the preservation of reactions that allow us to unravel diagenetic reactions and leads to the potential to identify primary precipitates that may link back to seawater chemistry at the time of formation.

IMPLICATIONS

Silica-cemented horizons in the Biwabik Iron Formation preserve Fe-rich silicate mineral assemblages and capture diagenetic reactions *in situ*. Because of this textural preservation, several inferences can be made regarding silica cementation and precursor sediment preservation in the Biwabik, which may extend to other post-GOE iron formations and provide potential insight into Paleoproterozoic seawater geochemistry. First and foremost, silica-cemented nodules preserve diagenetic reactions between iron silicate phases at nodule margins, revealing the effects of local geochemical exchange during diagenesis (Figure 10). Geochemical exchange during early diagenetic reactions modifies the composition of primary phases, complicating mineral composition-based precursor sediment interpretations. With the recent focus on early Fe-silicates in iron formations as proxies for seawater composition and redox conditions (e.g., Rasmussen et al. 2017; 2021), future studies should continue to constrain iron silicate mineral paragenesis using paired petrographic and geochemical approaches to identify effects of local geochemical exchange.

In silicified layers of the Biwabik Iron Formation, we identified texturally early greenalite that may represent the redox state of the precursor sediment, indicating primarily anoxic conditions existed in some parts of the basin where sufficient ferrous iron and silica were available for greenalite precipitation. Precipitation of a greenalite-like precursor sediment could have been driven by an increase in seawater pH (Tosca et al. 2016; Rasmussen et al. 2017) and/or a minor increase in available ferric iron that initiated iron silicate precipitation (Hinz et al. 2021). Though most hematite was observed to have mineralized after Fe-silicate phases when present in the same sample, a few noteworthy samples from specific stratigraphic intervals display hematite and chert as the earliest forming minerals (Basal Red and Upper Cherty, Figure 2) while lacking any texturally early iron silicates (e.g., Figure 9H). If these hematite samples represent precursor sediment precipitation under suboxic to oxic conditions, then perhaps precipitation of hematite and greenalite reflects mineral precipitation above and below a redoxcline, respectively. Similar oxygen-stratified depositional settings are suggested for other post-GOE Paleoproterozoic iron formation (Wilson et al. 2010; Akin et al. 2013; Pufahl et al. 2014). Since the Biwabik contains similar mineral assemblages as iron formations predating the GOE, future studies should continue to explore relationships between texturally early mineral phases and redox conditions of equilibrium assemblages. This approach - considering how paragenetic mineral assemblages can vary throughout iron formation stratigraphy (e.g. Beukes 1980), could help to clarify interpretations of redox conditions near the sediment/water interface for Precambrian iron formations where different proxies indicate disparate original oxidation states inferred to represent the time of deposition.

More broadly, it may be useful in future mineralogical studies of iron formation to consider textural relationships and mineral identification within silica-cemented horizons via combined transmitted and reflected light microscopy, electron microscopy, and spectroscopy techniques to gauge the effects of local geochemical exchange between bands during early diagenesis. Since geochemical exchange can affect early-forming mineral compositions while retaining primary mineral classification under the Laberge (1964) criteria, similar precaution should be taken for geochemical consideration of putative primary mineralogy in other Precambrian iron formations.

ACKNOWLEDGEMENTS

This work was funded by internal awards to L. Brengman from the University of Minnesota Duluth, and student research grants awarded to S. Duncanson from the Geological Society of America, and the Institute of Lake Superior Geology. We would like to specifically thank undergraduate students Stephen Hanson, Anthony Wetzel, and Kendall Johnson for sharing their help, time, and expertise as they each worked on their individual but related research projects. We would also like to thank Mark Severson, Mark Jirsa, and Phil Larson for introducing L. Brengman to the drill core repository, and for their helpful discussions over the last few years. We are grateful for helpful feedback from Maxwell Lechte and an anonymous reviewer, which has greatly improved this manuscript.

REFERENCES

Addison, W.D., Brumpton, G.R., Vallini, D.A., McNaughton, N.J., Davis, D.W., Kissin, S.A., Fralick, P.W., and Hammond, A.L. (2005) Discovery of distal ejecta from the 1850 Ma Sudbury impact event. Geology, 33, 193.

Akin, S.J., Pufahl, P.K., Hiatt, E.E., and Pirajno, F. (2013) Oxygenation of shallow marine environments and chemical sedimentation in Palaeoproterozoic peritidal settings: Frere Formation, Western Australia. (N. Sheldon, Ed.) Sedimentology, 60, 1559–1582.

Albut, G., Babechuk, M.G., Kleinhanns, I.C., Benger, M., Beukes, N.J., Steinhilber, B., Smith, A.J.B., Kruger, S.J., and Schoenberg, R. (2018) Modern rather than Mesoarchaean oxidative weathering responsible for the heavy stable Cr isotopic signatures of the 2.95 Ga old Ijzermijn iron formation (South Africa). Geochimica et Cosmochimica Acta, 228, 157–189.

Bekker, A., Slack, J.F., Planavsky, N., Krapez, B., Hofmann, A., Konhauser, K.O., and Rouxel, O.J. (2010) Iron Formation: The Sedimentary Product of a Complex Interplay among Mantle, Tectonic, Oceanic, and Biospheric Processes. Economic Geology, 105, 467–508.

Bekker, A., Planavsky, N.J., Krapež, B., Rasmussen, B., Hofmann, A., Slack, J.F., Rouxel, O.J., and Konhauser, K.O. (2014) Iron Formations: Their Origins and Implications for Ancient Seawater Chemistry. In Treatise on Geochemistry pp. 561–628. Elsevier.

Beukes, N.J. (1980). Lithofacies and stratigraphy of the Kuruman and Griquatown iron-formations, Northern Cape Province, South Africa. South African Journal of Geology, 83, 69-86.

Beukes, N.J., and Klein, C. (1990) Geochemistry and sedimentology of a facies transition — from microbanded to granular iron-formation — in the early Proterozoic Transvaal Supergroup, South Africa. Precambrian Research, 47, 99–139.

Brengman, L.A., Fedo, C.M., Whitehouse, M.J., Jabeen, I., and Banerjee, N.R. (2020) Textural, geochemical, and isotopic data from silicified rocks and associated chemical sedimentary rocks in the ~ 2.7 Ga Abitibi greenstone belt, Canada: Insight into the role of silicification. Precambrian Research, 351, 105946.

Dimroth, E., and Chauvel, J.-J. (1973) Petrography of the Sokoman Iron Formation in Part of the Central Labrador Trough, Quebec, Canada. GSA Bulletin, 84, 111–134.

Donovan, J.J., Allaz, J.M., von der Handt, A., Seward, G.G.E., Neill, O., Goemann, K., Chouinard, J., and Carpenter, P.K. (2021) Quantitative WDS compositional mapping using the electron microprobe. American Mineralogist, 106, 1717–1735.

Dove, P., and Rimstidt, J. (1994) Silica: physical behavior, geochemistry and materials applications. in "Silica-water interactions." Reviews in Mineral, 29.

Duncanson, S.P., (2020) Identification of Primary and Diagenetic Mineralogy Preserved in Silica-Cemented Horizons of the Biwabik Iron Formation, Minnesota, Using Petrography and Electron Microprobe Analysis, 120 p. M.Sc. thesis, University of Minnesota, Duluth.

Eyster, A., Brengman, L.A., Nichols, C.I.O., Levitt, Z., Wilcots, J., and Bergmann, K.D. (2021) A New Depositional Framework for Massive Iron Formations After the Great Oxidation Event. Geochemistry, Geophysics, Geosystems, 22.

Fischer, W.W., and Knoll, A.H. (2009) An iron shuttle for deepwater silica in Late Archean and early Paleoproterozoic iron formation. Geological Society of America Bulletin, 121, 222-235.

Floran, R.J., and Papike, J.J. (1975) Petrology of the low-grade rocks of the Gunflint Iron-Formation, Ontario-Minnesota. Geological Society of America Bulletin, 86, 1169–1190.

Floran, R.J., and Papike, J.J. (1978) Mineralogy and Petrology of the Gunflint Iron Formation, Minnesota-Ontario: Correlation of Compositional and Assemblage Variations at Low to Moderate Grade. Journal of Petrology, 19, 215–288.

Flügel, E., and Munnecke, A. (2010) Microfacies of carbonate rocks: analysis, interpretation and application, 2nd ed., 984 p. Springer, Heidelberg ; New York.

Fralick, P., Davis, D.W., and Kissin, S.A. (2002) The age of the Gunflint Formation, Ontario, Canada: single zircon U•Pb age determinations from reworked volcanic ash, 39, 11.

French, B.M. (1968) Bulletin No. 45. Progressive Contact Metamorphism of the Biwabik Iron-formation, Mesabi Range, Minnesota.

French, B.M. (1973) Mineral Assemblages in Diagenetic and Low-Grade Metamorphic Iron-Formation. Economic Geology, 68, 1063–1074.

Frost, C.D., von Blanckenburg, F., Schoenberg, R., Frost, B.R., and Swapp, S.M. (2007) Preservation of Fe isotope heterogeneities during diagenesis and metamorphism of banded iron formation. Contributions to Mineralogy and Petrology, 153, 211–235.

Gole, M.J. (1980) Mineralogy and petrology of very-low-metamorphic grade Archaean banded iron-formations, Weld Range, Western Australia. American Mineralogist, 65, 8–25.

Gumsley, A.P., Chamberlain, K.R., Bleeker, W., Söderlund, U., de Kock, M.O., Larsson, E.R., and Bekker, A. (2017) Timing and tempo of the Great Oxidation Event. Proceedings of the National Academy of Sciences, 114, 1811–1816.

Harder, H. (1978) Synthesis of Iron Layer Silicate Minerals under Natural Conditions. Clays and Clay Minerals, 26, 65–72.

Heaman, L.M., Easton, R.M. (2005) Proterozoic history of the Lake Nipigon area, Ontario: Constraints from U-Pb zircon and baddeleyite dating. 51st ILSG Annual Meeting, part 1, p. 24-25.

Heinrich, B., Urquhart, K., Arrott, A., Cochran, J., Myrtle, K., and Purcell, S. (1987) Ferromagnetic-resonance study of ultrathin bcc Fe (100) films grown epitaxially on fcc Ag (100) substrates. Physical review letters, 59, 1756.

Hemming, S., McLennan, S., Hanson, G., Krogstad, E., and Mezger, K. (1990) Pb isotope systematics in quartz. Eos, 71, 654–655.

Hinz, I.L., Nims, C., Theuer, S., Templeton, A.S., and Johnson, J.E. (2021) Ferric iron triggers greenalite formation in simulated Archean seawater. Geology, 49, 905-910.

Jiang, C.Z., and Tosca, N.J. (2019) Fe(II)-carbonate precipitation kinetics and the chemistry of anoxic ferruginous seawater. Earth and Planetary Science Letters, 506, 231–242.

Jirsa, M.A., Miller, J.D., and Morey, G.B. (2008) Geology of the Biwabik Iron Formation and Duluth Complex. Regulatory Toxicology and Pharmacology, 52, S5–S10.

Johnson, J.E., Muhling, J.R., Cosmidis, J., Rasmussen, B., and Templeton, A.S. (2018) Low-Fe(III) Greenalite Was a Primary Mineral From Neoarchean Oceans. Geophysical Research Letters, 45, 3182–3192.

Kipp, M.A., Stüeken, E.E., Bekker, A., and Buick, R. (2017) Selenium isotopes record extensive marine suboxia during the Great Oxidation Event. Proceedings of the National Academy of Sciences, 114, 875–880.

Klein, C. (2005) Some Precambrian banded iron-formations (BIFs) from around the world: Their age, geologic setting, mineralogy, metamorphism, geochemistry, and origins. American Mineralogist, 90, 1473–1499.

Konhauser, K.O., Planavsky, N.J., Hardisty, D.S., Robbins, L.J., Warchola, T.J., Haugaard, R., Lalonde, S.V., Partin, C.A., Oonk, P.B.H., Tsikos, H., and others (2017) Iron formations: A global record of Neoarchaean to Palaeoproterozoic environmental history. Earth-Science Reviews, 172, 140–177.

Krapež, B., Barley, M.E., and Pickard, A.L. (2003) Hydrothermal and resedimented origins of the precursor sediments to banded iron formation: sedimentological evidence from the Early Palaeoproterozoic Brockman Supersequence of Western Australia: Resedimented origins of banded iron formation. Sedimentology, 50, 979–1011.

LaBerge, G.L. (1964) Development of magnetite in iron formations of the Lake Superior region. Economic Geology, 59, 1313–1342.

Lafuente, B., Downs, R.T., Yang, H., and Stone, N. (2015) 1. The power of databases: The RRUFF project. In Highlights in mineralogical crystallography pp. 1–30. De Gruyter (O).

Lantink, M.L., Oonk, P.B., Floor, G.H., Tsikos, H., and Mason, P.R. (2018) Fe isotopes of a 2.4 Ga hematite-rich IF constrain marine redox conditions around the GOE. Precambrian Research, 305, 218–235.

Leith, C.K. (1903) The Mesabi iron-bearing district of Minnesota Vol. 43. US Government Printing Office.

Lucente, M.E., and Morey, G.B. (1983) Stratigraphy and sedimentology of the Lower Proterozoic Virginia Formation, northern Minnesota: Minnesota Geological Survey Report of Investigations 28, 28 p.

Losh, S., and Rague, R. (2018) Hydrothermal oxidation in the Biwabik Iron Formation, MN, USA. Mineralium Deposita, 53, 1143–1166.

Lowenstein, T.K., Kendall, B., and Anbar, A. (2013) The geologic history of seawater. In The Oceans and Marine Geochemistry pp. 569–622. Elsevier Inc.

Lyons, T.W., Reinhard, C.T., and Planavsky, N.J. (2014) The rise of oxygen in Earth’s early ocean and atmosphere. Nature, 506, 307–315.

Lyons, T.W., Diamond, C.W., Planavsky, N.J., Reinhard, C.T., and Li, C. (2021) Oxygenation, Life, and the Planetary System during Earth's Middle History: An Overview. Astrobiology, 21, 906–923.

Maliva, R.G., Knoll, A.H., and Simonson, B.M. (2005) Secular change in the Precambrian silica cycle: Insights from chert petrology. Geological Society of America Bulletin, 117, 835.

McSwiggen, P.L., and Morey, G.B. (2008) Overview of the mineralogy of the Biwabik Iron Formation, Mesabi Iron Range, northern Minnesota. Regulatory Toxicology and Pharmacology, 52, S11–S25.

Milesi, V., Guyot, F., Brunet, F., Richard, L., Recham, N., Benedetti, M., Dairou, J., and Prinzhofer, A. (2015) Formation of CO2, H2 and condensed carbon from siderite dissolution in the 200–300°C range and at 50MPa. Geochimica et Cosmochimica Acta, 154, 201–211.

Morey, G.B. (1992) Chemical composition of the eastern Biwabik Iron-Formation (early Proterozoic), Mesabi Range, Minnesota. Economic Geology, 87, 1649–1658.

Muhling, J.R., and Rasmussen, B. (2020) Widespread deposition of greenalite to form Banded Iron Formations before the Great Oxidation Event. Precambrian Research, 339, 105619.

Ojakangas, R.W. (1983) Tidal deposits in the early Proterozoic basin of the Lake Superior region—The Palms and the Pokegama Formations: Evidence for subtidal-shelf deposition of Superior-type banded iron-formation. Geological Society of America Memoir, 160, 49–66.

Ojakangas, R.W., Morey, G.B., and Southwick, D.L. (2001) Paleoproterozoic basin development and sedimentation in the Lake Superior region, North America. Sedimentary Geology, 141–142, 319–341.

Ojakangas, R.W., Severson, M.J., and Jongewaard, P.K. (2011) Geology and sedimentology of the Paleoproterozoic Animikie Group: The Pokegama Formation, the Biwabik Iron Formation, and Virginia Formation of the eastern Mesabi Iron Range and Thomson Formation near Duluth, northeastern Minnesota. In Archean to Anthropocene: Field Guides to the Geology of the Mid-Continent of North America pp. 101–120. Geological Society of America.

Pecoits, E., Gingras, M.K., Barley, M.E., Kappler, A., Posth, N.R., and Konhauser, K.O. (2009) Petrography and geochemistry of the Dales Gorge banded iron formation: Paragenetic sequence, source and implications for palaeo-ocean chemistry. Precambrian Research, 172, 163–187.

Planavsky, N., Rouxel, O., Bekker, A., Shapiro, R., Fralick, P., and Knudsen, A. (2009) Iron-oxidizing microbial ecosystems thrived in late Paleoproterozoic redox-stratified oceans. Earth and Planetary Science Letters, 286, 230–242.

Planavsky, N.J., Bekker, A., Hofmann, A., Owens, J.D., and Lyons, T.W. (2012) Sulfur record of rising and falling marine oxygen and sulfate levels during the Lomagundi event. Proceedings of the National Academy of Sciences, 109, 18300–18305.

Posth, N.R., Köhler, I., D. Swanner, E., Schröder, C., Wellmann, E., Binder, B., Konhauser, K.O., Neumann, U., Berthold, C., Nowak, M., and others (2013) Simulating Precambrian banded iron formation diagenesis. Chemical Geology, 362, 66–73.

Pouchou, J.-L., and Pichoir, F. (1991) Quantitative analysis of homogeneous or stratified microvolumes applying the model “PAP.” In Electron probe quantitation pp. 31–75. Springer.

Poulton, S.W., Bekker, A., Cumming, V.M., Zerkle, A.L., Canfield, D.E., and Johnston, D.T. (2021) A 200-million-year delay in permanent atmospheric oxygenation. Nature, 592, 232–236.

Pufahl, P.K., Anderson, S.L., and Hiatt, E.E. (2014) Dynamic sedimentation of Paleoproterozoic continental margin iron formation, Labrador Trough, Canada: Paleoenvironments and sequence stratigraphy. Sedimentary Geology, 309, 48–65.

Rasmussen, B., and Muhling, J.R. (2018) Making magnetite late again: Evidence for widespread magnetite growth by thermal decomposition of siderite in Hamersley banded iron formations. Precambrian Research, 306, 64–93.

——— (2020) Hematite replacement and oxidative overprinting recorded in the 1.88 Ga Gunflint iron formation, Ontario, Canada. Geology, 48, 688-692.

Rasmussen, B., Meier, D.B., Krapež, B., and Muhling, J.R. (2013) Iron silicate microgranules as precursor sediments to 2.5-billion-year-old banded iron formations. Geology, 41, 435–438.

Rasmussen, B., Krapez, B., and Meier, D.B. (2014) Replacement origin for hematite in 2.5 Ga banded iron formation: Evidence for postdepositional oxidation of iron-bearing minerals. Geological Society of America Bulletin, 126, 438–446.

Rasmussen, B., Krapež, B., and Muhling, J.R. (2015) Seafloor silicification and hardground development during deposition of 2.5 Ga banded iron formations. Geology, 43, 235–238.

Rasmussen, B., Muhling, J.R., Suvorova, A., and Krapež, B. (2016) Dust to dust: Evidence for the formation of "primary" hematite dust in banded iron formations via oxidation of iron silicate nanoparticles. Precambrian Research, 284, 49–63.

——— (2017) Greenalite precipitation linked to the deposition of banded iron formations downslope from a late Archean carbonate platform. Precambrian Research, 290, 49–62.

Rasmussen, B., Muhling, J.R., and Fischer, W.W. (2019) Evidence from laminated chert in banded iron formations for deposition by gravitational settling of iron-silicate muds. Geology, 47, 167–170.

Rasmussen, B., Muhling, J.R., and Krapež, B. (2021) Greenalite and its role in the genesis of early Precambrian iron formations – A review. Earth-Science Reviews, 103613.

Robbins, L.J., Funk, S.P., Flynn, S.L., Warchola, T.J., Li, Z., Lalonde, S.V., Rostron, B.J., Smith, A.J.B., Beukes, N.J., de Kock, M.O., and others (2019) Hydrogeological constraints on the formation of Palaeoproterozoic banded iron formations. Nature Geoscience, 12, 558–563.

Schneider, C.A., Rasband, W.S., and Eliceiri, K.W. (2012) NIH Image to ImageJ: 25 years of image analysis. Nature Methods, 9, 671–675.

Schulz, K.J., and Cannon, W.F. (2007) The Penokean orogeny in the Lake Superior region. Precambrian Research, 157, 4–25.

Severson, M.J., Heine, J.J., and Patelke, M.M. (2009) Geologic and Stratigraphic Controls of the Biwabik Iron Formation and the Aggregate Potential of the Mesabi Iron Range, Minnesota. University of Minnesota Duluth, Natural Resources Research Institute, Technical Report NRRI/TR-2009/09, 173 p. + 37 plates.

Sheppard, S., Krapež, B., Zi, J.-W., Rasmussen, B., and Fletcher, I.R. (2017) Young ores in old rocks: Proterozoic iron mineralisation in Mesoarchean banded iron formation, northern Pilbara Craton, Australia. Ore Geology Reviews, 89, 40–69.

Siever, R. (1992) The silica cycle in the Precambrian. Geochimica et Cosmochimica Acta, 56, 3265–3272.

Simonson, B.M., (1987) Early Silica Cementation and Subsequent Diagenesis in Arenites from Four Early Proterozoic Iron Formations of North America. SEPM Journal of Sedimentary Research, 57, 494–511.

Southwick, D., and Day, W. (1983) Geology and petrology of Proterozoic mafic dikes, north-central Minnesota and western Ontario. Canadian Journal of Earth Sciences, 20, 622–638.

Stefurak, E.J.T., Lowe, D.R., Zentner, D., and Fischer, W.W. (2014) Primary silica granules—A new mode of Paleoarchean sedimentation. Geology, 42, 283–286.

——— (2015) Sedimentology and geochemistry of Archean silica granules. Geological Society of America Bulletin, 127, 1090–1107.

Sturesson, U., Heikoop, J.M., and Risk, M.J. (2000) Modern and Palaeozoic iron ooids—a similar volcanic origin. Sedimentary Geology, 136, 137–146.

Todd, S.E., Pufahl, P.K., Murphy, J.B., and Taylor, K.G. (2019) Sedimentology and oceanography of Early Ordovician ironstone, Bell Island, Newfoundland: Ferruginous seawater and upwelling in the Rheic Ocean. Sedimentary Geology, 379, 1–15.

Tosca, N.J., Guggenheim, S., and Pufahl, P.K. (2016) An authigenic origin for Precambrian greenalite: Implications for iron formation and the chemistry of ancient seawater. Geological Society of America Bulletin, 128, 511–530.

Tosca, N.J., Jiang, C.Z., Rasmussen, B., and Muhling, J. (2019) Products of the iron cycle on the early Earth. Free Radical Biology and Medicine, 140, 138-153.

van de Velde, S.J., Reinhard, C.T., Ridgwell, A., and Meysman, F.J. (2020) Bistability in the redox chemistry of sediments and oceans. Proceedings of the National Academy of Sciences, 117, 33043–33050.

Wacey, D., Eiloart, K., and Saunders, M. (2021) Pathways of microfossil mineralisation by hematite in the 1878 Ma Gunflint Formation. Chemical Geology, 581, 120419.

Wilson, J.P., Fischer, W.W., Johnston, D.T., Knoll, A.H., Grotzinger, J.P., Walter, M.R., McNaughton, N.J., Simon, M., Abelson, J., Schrag, D.P., and others (2010) Geobiology of the late Paleoproterozoic Duck Creek Formation, Western Australia. Precambrian Research, 179, 135–149.

Wintsch, R.P., and Kvale, C.M. (1994) Differential Mobility of Elements in Burial Diagenesis of Siliciclastic Rocks. SEPM Journal of Sedimentary Research, 64A, 349–361.

Wolff, J. (1917) Recent geologic developments on the Mesabi iron range, Minnesota. American Institute of Mining and Metallurgical Engineers, Transactions, 56, p. 229-257.

Figure Captions

Figure 1. Mineralogy studies identifying primary Fe-silicates among silica-cemented horizons in iron formations through Earth history. (A) Si-cement study references come from Rasmussen and Muhling (2021), and are 1= Rasmussen et al. (2014b); 2= Muhling and Rasmussen (2020) 3= Sheppard et al. (2017); 4= Rasmussen et al. (2015); 5= Rasmussen et al. (2017); 6= Beukes (1980), 7= Tosca et al. (2019); 8= Lantink et al. (2018). (B) Atmospheric oxygen concentrations from Lyons et al. 2021. (C) Simplified ocean chemistry adapted from Lowenstein et al. (2013) and van de Velde et al. (2020). (D) Distribution of marine iron formation deposits in billion metric tons (Gt), modified from Bekker et al. (2014), based on data from Bekker et al. (2010.) Asterix and lighter color boxes represent units with poor age constraints.

Figure 2. Simplified Archean-Proterozoic bedrock geology of Northeastern Minnesota including Mesabi and Gunflint Iron Ranges. The star denotes location of drill cores sampled for this study. Modified from Jirsa et al. (2007) and Poulton et al. (2010). (A) Regional schematic showing the geographic location of the Animikie Basin and associated Mesabi iron range. (B) Simplified geologic map showing the relationship between rocks of the Animikie Basin and surrounding rocks. (C) Graphic log of drill cores LWD-99-01 and LWD-99-02 from the star locations in B. Petrography samples denoted by circle symbols, stars represent samples with EPMA data. Depth is noted as feet and as meters below surface. Drill core logs based on observational data and Severson et al. (2009.)

Figure 3. Example of a silica-cemented horizons in the Biwabik Iron Formation. (A) Drill core showing a chert nodule and the surrounding fine-grained, banded horizons. Note the sediment

draping around a silica nodule. The sample comes from the Lower Cherty, a unit defined by granular textures overall. (B) Photomicrograph composite map of the same chert nodule as (A). The chert nodule preserves granular textures and quartz cement. Within silica-cemented nodules, a higher density of iron phases between granules are often observed proximal to the banded horizons (nodule margin) relative to the nodule center. (C) Drill core photo showing chert nodule and surrounding thin banded horizons. (D) Close up photomicrograph composite map of the area outlined by the square in (C) showing preservation of granular textures in silica-cemented nodules. The sample comes from the Lower Cherty, a unit that predominantly contains banded textures.

Figure 4. Electron microprobe point data from chamosite (A), stilpnomelane (B), minnesotaite (C) and greenalite (D). Samples are separated based on mineralogy and textural relationships (described in the text), and "n" refers to the number of point analyses per sample.

Figure 5. Representative examples of chamosite textures preserved in silica-cemented horizons and banded horizons. (A) Si-cemented horizon (sample MIR-19-12) showing zonation (zones 1-3). Granules in zones 1 and 3 are predominantly chamosite, while granules in zone 2 have less chamosite, and are primarily composed of chert. (B) Photomicrograph showing chamosite (chm) occurring as granules in Si-cemented (qtz) and banded horizons (sample MIR-19-15). Granules near the banded horizon often contain stilpnomelane (stp) as well (C) Plane-polarized light photomicrograph showing chamosite occurring within banded horizons (sample MIR-19-15). (D) Back-scattered electron image showing chamosite (chm) and a carbonate crystal (cb) cross-cut by stilpnomelane (stp).

Figure 6. Representative examples of minnesotaite textures preserved in Si-cemented horizons. (A) Cross-polarized light photomicrograph composite map of sample MIR-L-07 showing granular vs. banded textures. (B) Close-up photomicrograph of square in (A) showing greenalite granules with minnesotaite (mns) as cement and intergranular phases (sample MIR-L-07). (C) Composite photomicrograph (cross-polarized light) of sample MIR-19-05 showing minnesotaite granules. (D) Close up of square in (C) of minnesotaite granule (mns 1) and cement (mns 2). Note cross-cutting magnetite (mt). (E) Plane-polarized light photomicrograph composite map of Si-cemented horizons (chert nodule) in sample MIR-19-3.5. (F) Back-scattered electron image of minnesotaite (mns) granule preserved inside the Si-cemented horizon in (D). (G) Back-scattered electron image of stilpnomelane (stp) granule preserved at the edge of the chert nodule (D), near the banded layer. Note the cross-cutting relationship between magnetite (mt) and stilpnomelane (stp).

Figure 7. Representative examples of greenalite textures and greenalite-minnesotaite textural relationships preserved in Si-cemented horizons and Raman spectra of greenalite and minnesotaite. (A) Plane-polarized light composite photomicrograph map of sample MIR-U-10. (B) Close-up, plane-polarized light photomicrograph map of square area in (A) showing greenalite granules. (C) Back-scattered electron image of square area in (B) showing greenalite granules. (D and E) Close-up back-scattered electron images of square areas in (C) showing greenalite granule (gre) and minnesotaite cement (mns in D) as well as minor compositional

variation (x) internal to greenalite (gre) granules (E)). (F) Back-scatter electron image of granules composed of greenalite aggregates (gre) and minnesotaite (mns) cement (sample MIR-L-07)). (G) Close-up back-scattered electron image of square area in (F) showing greenalite granule (gre) and minnesotaite cement (mns) growing into non-compaction fracture (now quartz-cemented, arrows). (H) Raman spectra for areas 1 (mns) and 2 (gre) in (D) and 3 (mns) and 4 (gre) in (G).

Figure 8. Additional examples of greenalite textures and greenalite-minnesotaite textural relationships preserved in Si-cemented horizons with Raman spectra across a granule-cement transect. (A) Cross-polarized light composite photomicrograph map of sample MIR-17-13 showing mixed greenalite-minnesotaite granules. (B) Back-scattered electron image of square area in (A) containing granules composed of greenalite and acicular minnesotaite among dark-gray quartz cement. (C) Back-scattered electron image of granule with minnesotaite (mns) cement nucleating off granule boundaries (sample MIR-17-13). (D) Close-up photomicrograph of rectangle in (B). (E) Raman spectra transect across granule-cement contact (numbered line in D)). (F) Mineral map of Raman spectra from area (F) showing both primarily greenalite and mixed greenalite-minnesotaite granules with minnesotaite and quartz cement. (G) Cherty granule with dusty appearance due to presence of disseminated sub μm greenalite crystals (sample MIR-17-18). (H) Back-scattered electron image of square area in (G) showing fine-grained, disseminated Fe-oxides and greenalite next to a quartz filled non-compaction fracture (qtz ncf). (I) Composite SEM K-alpha element map acquired with EDS showing Fe and Si distributions in the same field of view as (H).

Figure 9. Representative examples of cross-cutting relationships between carbonates, Fe-oxides, and silicate phases. (A) Cross-polarized photomicrograph showing large, euhedral carbonate, and > 5 μm hematite laths cross-cutting chert granules. (B) Back-scattered electron image showing an example of minnesotaite (mns) cross-cutting carbonates (carb.) with variable Ca-Fe-Mg composition (white dashed lines and black dashed lines). (C) Plane-polarized light photomicrograph showing a chert intraclast with carbonate crystals (carb.) inside the intraclast. (D) Cross-polarized light photomicrograph of a different chert intraclast with carbonate crystals (carb.; larger than those in C). (E) Altered granule showing magnetite (mt) cross-cutting minnesotaite (mns) and carbonate (carb.), forming rims around replaced granules. (F) Back-scattered electron image showing >5 μm hematite laths and fine-grained hematite (hm, arrows), and large, euhedral magnetite (mt) cross-cutting fine-grained iron silicate phases (chamosite, chm). Stilpnomelane (stp) is also shown cross-cutting chamosite (chm) in the same image). (G) Close-up image of phase relationships demonstrated in (F). (H) Back-scattered electron image of a quartz grain (qtz) coated with multiple layers of fine-grained hematite (hm).

Figure 10. Proposed diagenetic model for Fe-silicate mineral assemblages in the Biwabik Iron Formation. (A) Initial sediment deposition includes mixed $Fe^{2+,3+}$-Si-O-OH gel, terrigenous-sourced sediment, and the possibility for addition of Si through diffusion of silicic acid (H_4SiO_4) into the sediment. (B) Post-deposition, but still during early diagenesis, several different mineral reaction sets may take place (B_1-B_3) depending on the nature and degree of silica-addition through silicification, and original presence of terrigenous sediment. References for reactions outlined in sequences B_1- B_3 are as follow: (1,2) Posth et al. 2013; (3) French 1973; (4) Tosca et al. 2019; (5) Milesi et al. 2015; Rasmussen et al. 2018; (6) Dove and Rimstidt 1994; (7) Klein

2005; this study; (8) Gole 1980; (9) Tosca et al. 2016; (10) Klein 2005; (11) Floran and Papike 1978. (C) Reactions from (B) lead to the present mineralogy observed in the sample sets. Minerals and sediments are not to scale.

Supplementary Figure S1 caption.

Figure S1. Summary of locations and mineralogy of individual EPMA point analyses in thin section samples MIR-17-21, MIR-17-19, MIR-U-10 and MIR-17-16. (A-D) TL images of samples. (E-H): BSE images of point analysis areas. The chert intraclast in H is traced with a dashed outline. (I) FeO-MgO-Cao ternary diagram. Gray-colored triangles are from two carbonate-bearing rock types in the Stambaugh Formation (Planavsky et al. 2018).

Table 1. Samples for electron probe microanalysis.

Unit	Sample	Core ft.	Mineral phase(s) targeted for EPMA point analysis	General description of phase for EPMA point analysis
Upper Slaty	MIR-17-18	587'	chamosite, siderite, ankerite-dolomite	(1) Chamosite granules in banded horizon (2) carbonate rhombs in chert intraclast (3) carbonate phases among veins
	MIR-17-16	617'	stilpnomelane	Stilpnomelane crystals in chert intraclast
	MIR-17-15	622'	chamosite	Chamosite granules among banded horizons
Upper Cherty	MIR-19-15 (99-2)	872'	chamosite	Chamosite granules among silica-cemented and banded horizons
	MIR-17-13	647'	minnesotaite	(1) Granules among silica-cement (2) Minnesotaite cement
Lower Slaty	MIR-19-05	889'	minnesotaite	(1) Granules among silica-cement (2) Minnesotaite cement
	U-07	893'	siderite	Carbonate rhombs encrusted in magnetite
	U-08	908'	stilpnomelane, minnesotaite	(1) Stilpnomelane granules among banded horizon (2) Minnesotaite granules among silica-cement
Lower Cherty	U-10	1060'	greenalite, minnesotaite, siderite	(1) Greenalite granules (2) Micritic siderite (3) Minnesotaite cement
	L-07	1221'	greenalite, minnesotaite	(1) Greenalite granules (2) Minnesotaite cement
	MIR-19-12 (99-2)	1394'	chamosite	Granules inside and outside silica-cemented nodule
	MIR-19-3.5	1247'	stilpnomelane, minnesotaite	(1) Minnesotaite granules inside silica-cemented nodule (2) Stilpnomelane granules among edge of nodule

Table 2. The typical habits and distribution of common minerals among silica-cemented and banded horizons.

Mineral	**Crystal habit**	**Distribution among silica-cemented and banded horizons**
Fe-silicates		
Greenalite	sub-µm crystals, appearing within granules as either disseminated crystals floating among chert or as aggregates of greenalite crystals	Internally within granules among silica- cemented horizons
Chamosite	aggregates of sub-µm crystals within granules	Internally within granules among silica-cemented and banded horizons
Minnesotaite	~3-50 µm euhedral-subhedral acicular sheaves within granules and among pore space	Within granules and as interstitial cement in silica-cemented horizons
Stilpnomelane	~3-100 µm acicular crystals within granules and among pore space	Within granules and as interstitial cement in silica-cemented and banded horizons
Carbonates		
Calcite	~5-15 µm micritic cement	Non-granular iron formation carbonate horizon
Ankerite-dolomite	~5-15 µm micritic cement, ~0.1 - 5 mm euhedral-subhedral rhombohedral	Micritic cement among banded horizons, rhombohedral among silica-cemented and banded horizons
Siderite	~5-15 µm micritic cement, ~100µm - 5 mm euhedral-subhedral rhombohedral	Micritic cement among banded horizons, rhombohedral among silica-cemented and banded horizons
Fe-oxides		
Hematite	sub-µm crystals, or as ≥5 µm subhedral plates	Both habits found among silica-cemented and banded horizons
Magnetite	~10-20 µm euhedral cubes	Found among silica-cemented and banded horizons

Table 3. Electron Microprobe analyses of average Fe-silicate composition and formulae ions.

	Chamosite				**Minnesotaite**						**Stilpnomelane**			**Greenalite**	
Sample (MIR)	**17-15**	**17-18**	**19-12**	**19-15**	**L-07**	**U-10**	**17-13**	**19-05**	**19-3.5**	**U-08**	**19-3.5**	**U-08**	**17-16**	**L-07**	**U-10**
# of points (n)	n = 20	n = 11	n = 20	n = 17	n = 14	n = 2	n = 22	n = 25	n = 13	n = 5	n = 6	n = 8	n = 3	n = 10	n = 10
Na_2O	0.04	0.03	0.03	0.1	0.03	0.04	0.01	0	0.06	0.02	0.37	0.18	0.43	0.06	0.05
MgO	4.02	5.92	7.37	13.55	6.73	4.24	1.63	7.33	19.5	19.75	10.84	12.77	3.01	5.86	3.11
SiO_2	24.83	24.36	25.02	29.72	53.37	51.94	49.09	52.73	56.21	56.78	42.84	48.59	46.93	34.35	33.35
Al_2O_3	13.93	16.74	15.9	11.7	0.64	0.23	0.23	0.11	0.56	0.47	3.45	4.32	4.54	2.32	0.95
K_2O	0.02	0.02	0	0.13	0.35	0.16	0.09	0.06	0.11	0.05	1.82	1.09	1.75	0.03	0.01
CaO	0.15	0.05	0.14	0.17	0.01	-0.02	0.04	0	0.11	0.04	0.04	0.05	0.04	0.18	0.18
FeO	43.78	40.52	38.79	30.54	32.55	36.88	42.21	32.88	17.2	16.61	25.85	24.84	33.58	44.61	51.18
MnO	0.08	0.03	0.16	0.2	0.09	0.14	0.04	0.05	0.03	0.02	0.17	0.1	0.15	0.16	0.27
O	0	9.48	10.24	10.71	5.33	7.34	5.63	5.23	4.7	4.44	15.76	7.92	8.73	7.97	8.67
Oxide total	99.80	97.13	97.66	96.82	99.1	100.93	98.99	98.4	98.49	98.17	101.14	99.88	99.15	95.55	97.77
Average formula															
Si	2.96	2.81	2.86	3.32	4.08	4.06	3.94	4.04	3.92	3.95	3.41	3.57	3.82	4.14	4.06
Fe	4.36	3.9	3.72	2.86	2.08	2.41	2.84	2.11	1	0.97	1.72	1.53	2.28	4.49	5.22
Mg	0.71	1.02	1.26	2.26	0.77	0.49	0.19	0.84	2.03	2.05	1.29	1.4	0.21	1.04	0.56
Mn	0.01	0	0.02	0.02	0.01	0.01	0	0	0	0	0.01	0.01	0.01	0.02	0.03
Al	1.96	2.27	2.15	1.54	0.06	0.02	0.02	0.01	0.05	0.04	0.32	0.37	0.43	0.32	0.14
K	-	-	-	-	-	-	-	-	-	-	0.19	0.1	0.18	-	-
Na	-	-	-	-	-	-	-	-	-	-	0.06	0.03	0.07	-	-
O	10	10	10	10	10	10	10	10	10	10	12	12	12	10	10
(OH)	8	8	8	8	2	2	2	2	2	2	1	1	1	8	8

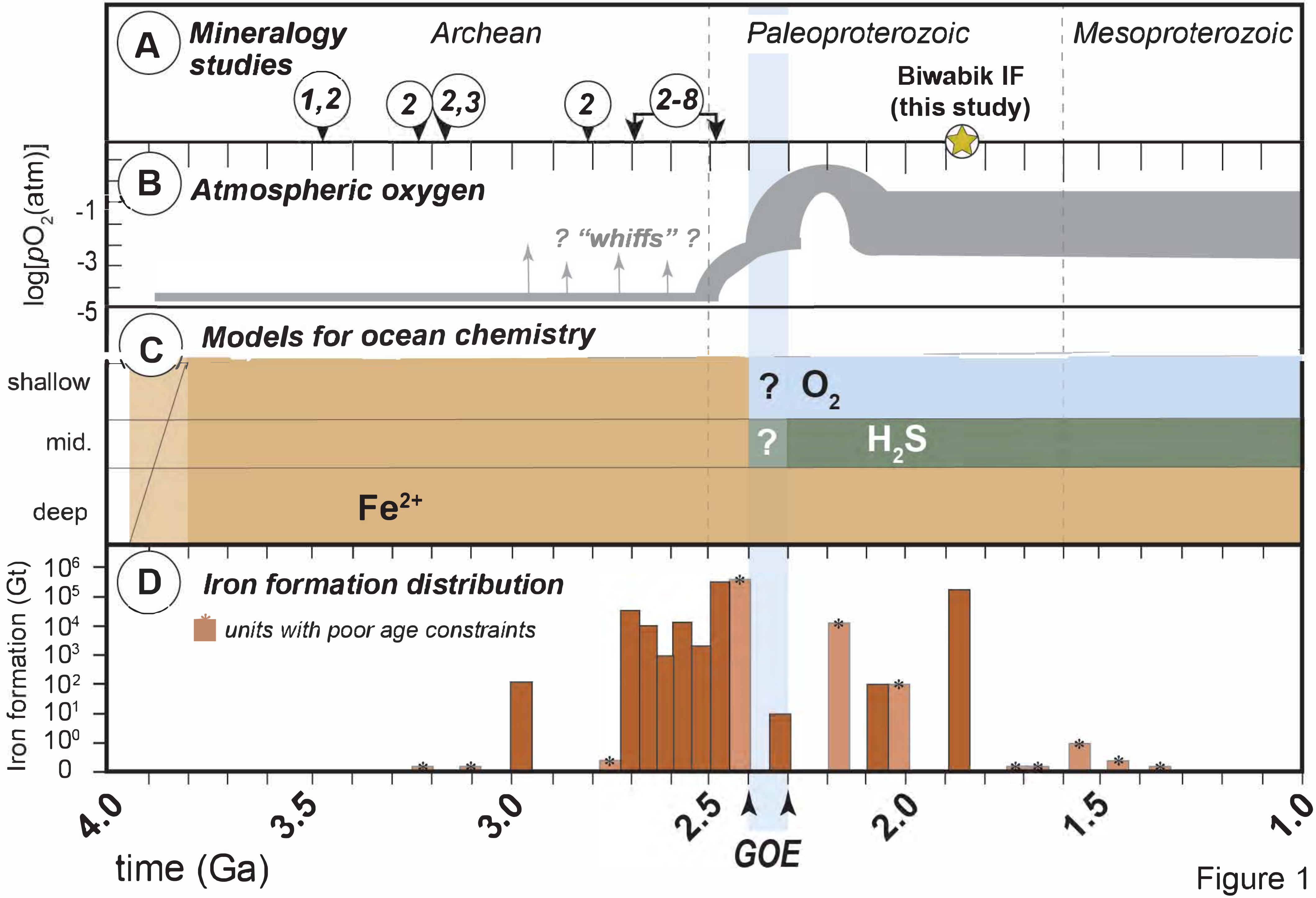
A
Mineralogy studies
Archean
Paleoproterozoic
Mesoproterozoic
1,2
2
2,3
2
2-8
Biwabik IF (this study)
B
Atmospheric oxygen
log[pO_2(atm)]
-1
-3
-5
? "whiffs" ?
C
Models for ocean chemistry
shallow
mid.
deep
? O_2
? H_2S
Fe^{2+}
D
Iron formation distribution
units with poor age constraints
Iron formation (Gt)
10^6
10^5
10^4
10^3
10^2
10^1
10^0
0
*
4.0
3.5
3.0
2.5
2.0
1.5
1.0
GOE
time (Ga)

Figure 1

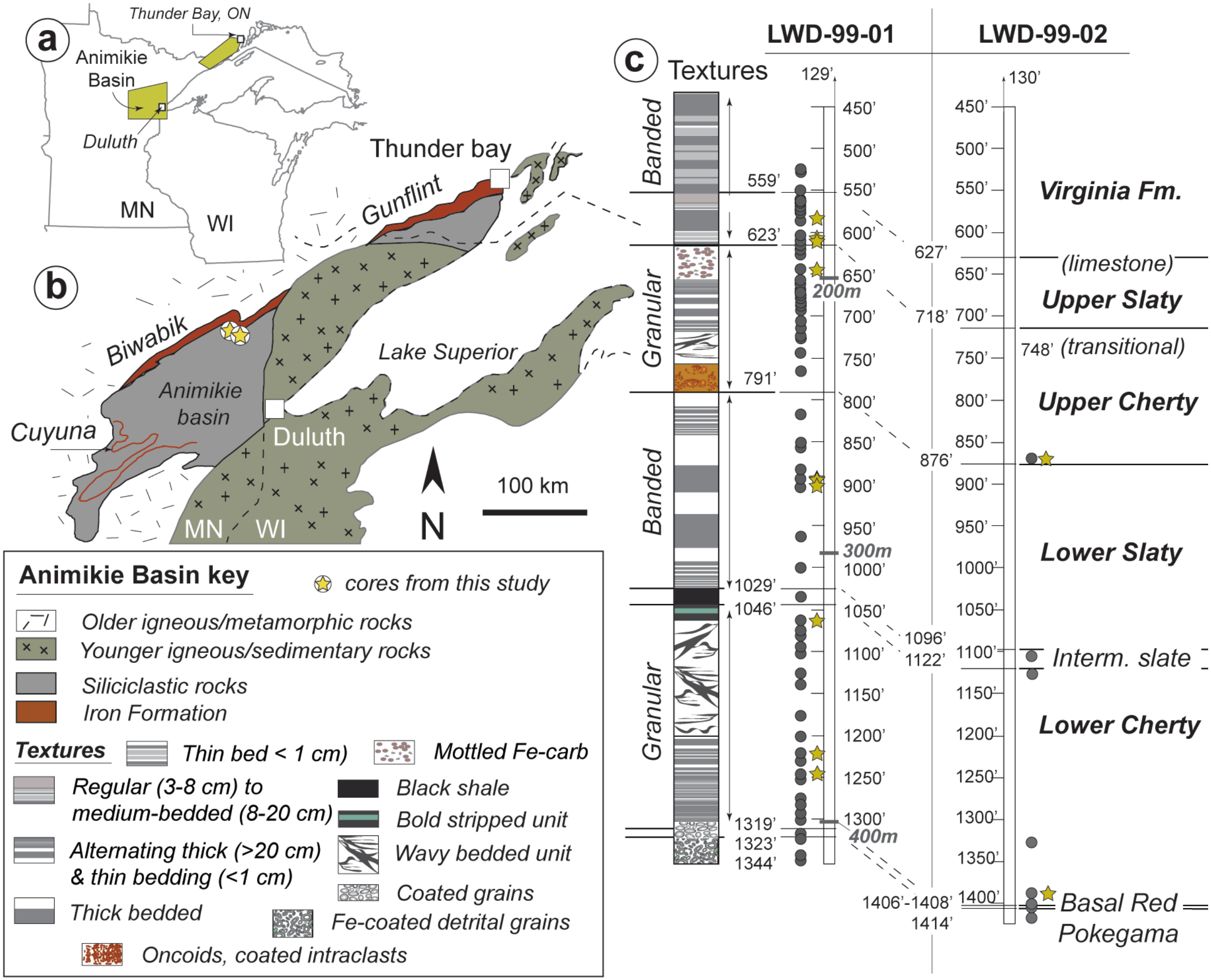
a
Thunder Bay, ON
Animikie Basin
Duluth
MN
WI
b
Thunder bay
Gunflint
Biwabik
Cuyuna
Animikie basin
Duluth
Lake Superior
MN
WI
N
100 km
Animikie Basin key
cores from this study
Older igneous/metamorphic rocks
Younger igneous/sedimentary rocks
Siliciclastic rocks
Iron Formation
Textures
Thin bed < 1 cm)
Mottled Fe-carb
Regular (3-8 cm) to medium-bedded (8-20 cm)
Black shale
Bold stripped unit
Alternating thick (>20 cm) & thin bedding (<1 cm)
Wavy bedded unit
Thick bedded
Coated grains
Fe-coated detrital grains
Oncoids, coated intraclasts
c
Textures
LWD-99-01
LWD-99-02
Banded
Granular
Banded
Granular
129'
130'
559'
623'
791'
1029'
1046'
1319'
1323'
1344'
450'
500'
550'
600'
650'
700'
750'
800'
850'
900'
950'
1000'
1050'
1100'
1150'
1200'
1250'
1300'
1350'
1400'
200m
300m
400m
627'
718'
876'
1096'
1122'
748'
1406'-1408'
1414'
Virginia Fm.
(limestone)
Upper Slaty
(transitional)
Upper Cherty
Lower Slaty
Interm. slate
Lower Cherty
Basal Red
Pokegama

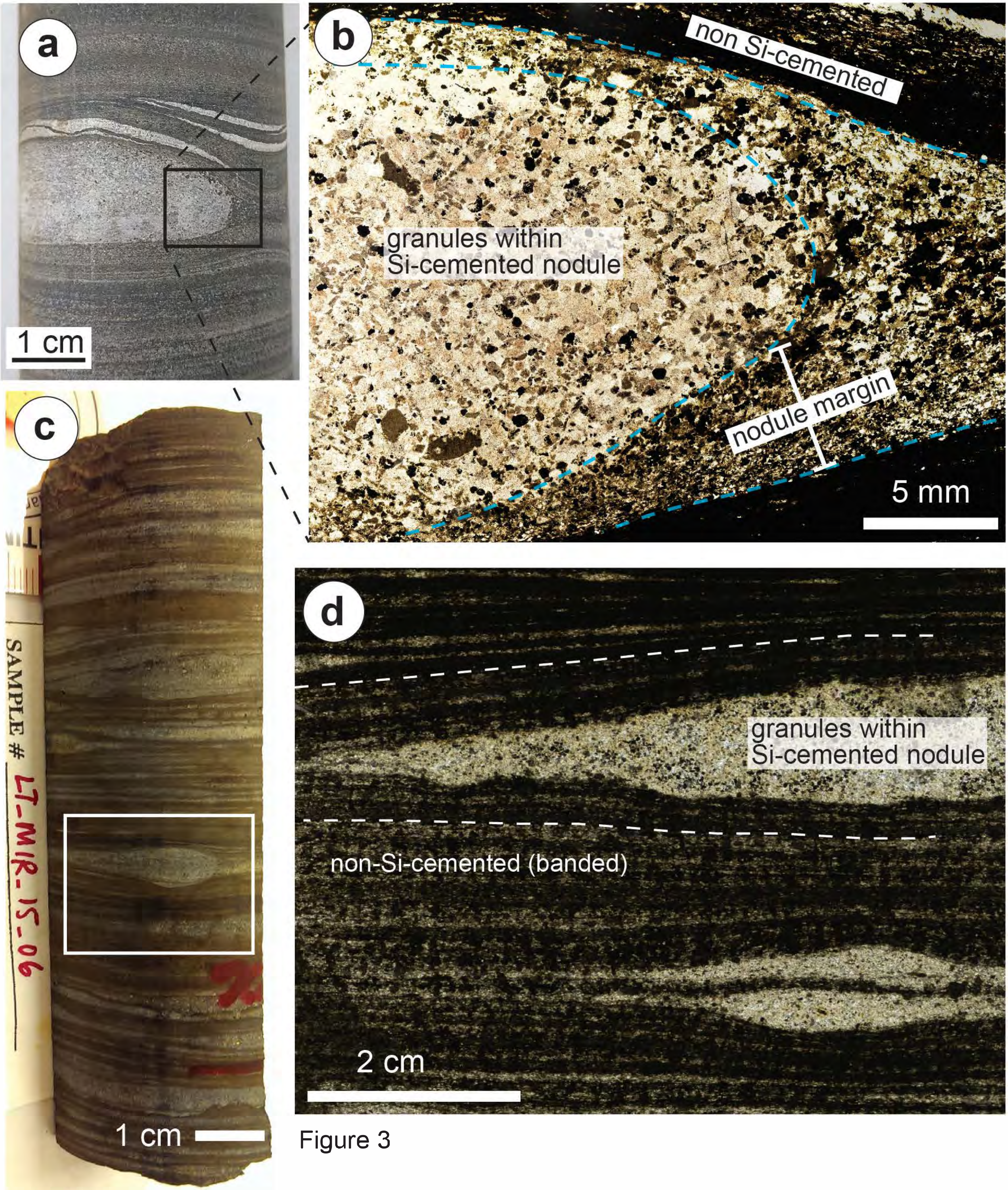
a
1 cm
b
non Si-cemented
granules within
Si-cemented nodule
nodule margin
5 mm
c
SAMPLE # LT-MIR_15_06
1 cm
d
granules within
Si-cemented nodule
non-Si-cemented (banded)
2 cm

Figure 3

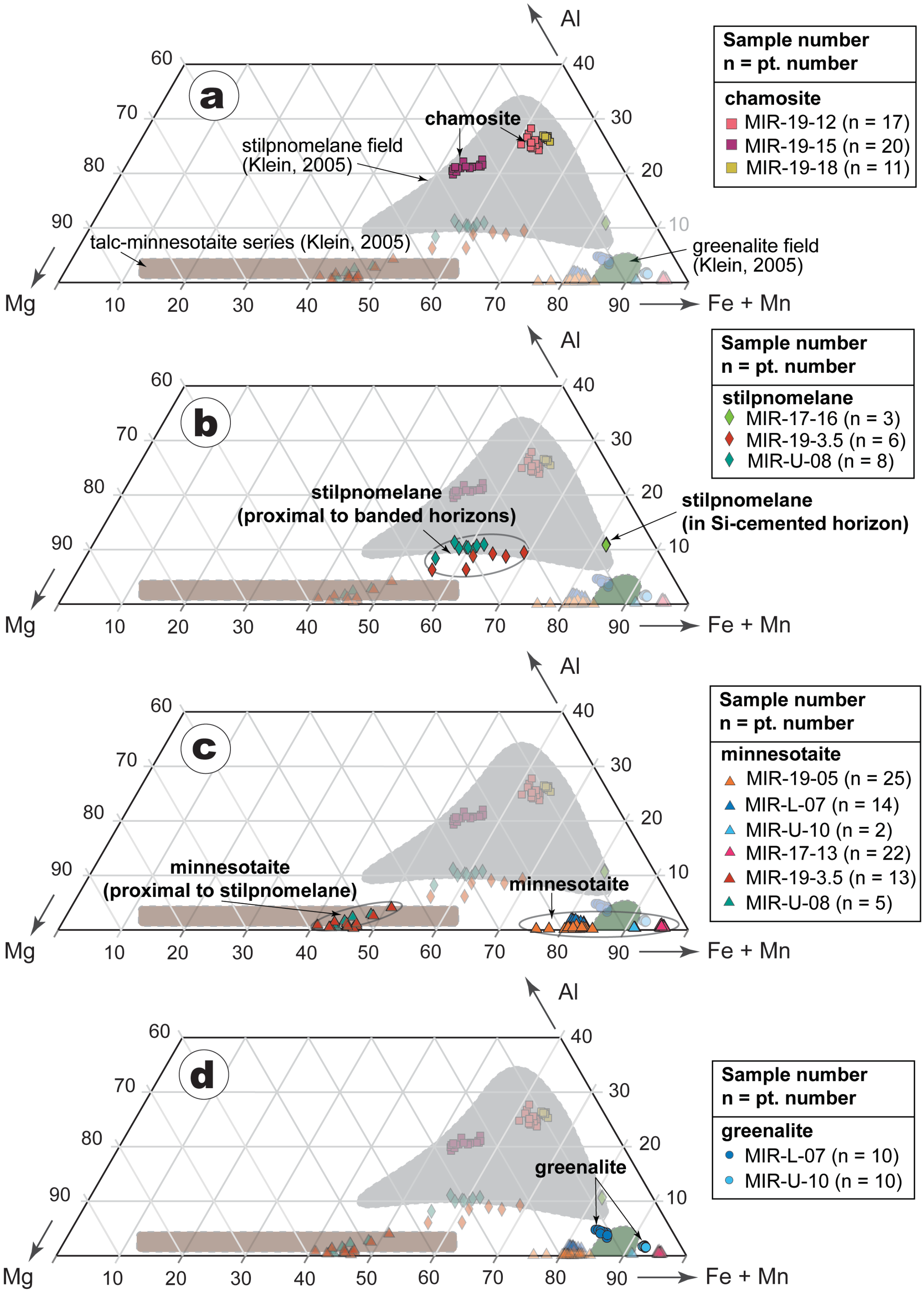
a
Al
Mg
Fe + Mn
10
20
30
40
50
60
70
80
90
60
70
80
90
40
30
20
10
chamosite
stilpnomelane field
(Klein, 2005)
talc-minnesotaite series (Klein, 2005)
greenalite field
(Klein, 2005)
Sample number
n = pt. number
chamosite
■ MIR-19-12 (n = 17)
■ MIR-19-15 (n = 20)
■ MIR-19-18 (n = 11)
b
stilpnomelane
(proximal to banded horizons)
stilpnomelane
(in Si-cemented horizon)
Sample number
n = pt. number
stilpnomelane
◆ MIR-17-16 (n = 3)
◆ MIR-19-3.5 (n = 6)
◆ MIR-U-08 (n = 8)
c
minnesotaite
(proximal to stilpnomelane)
minnesotaite
Sample number
n = pt. number
minnesotaite
▲ MIR-19-05 (n = 25)
▲ MIR-L-07 (n = 14)
▲ MIR-U-10 (n = 2)
▲ MIR-17-13 (n = 22)
▲ MIR-19-3.5 (n = 13)
▲ MIR-U-08 (n = 5)
d
greenalite
Sample number
n = pt. number
greenalite
● MIR-L-07 (n = 10)
● MIR-U-10 (n = 10)

Figure 5

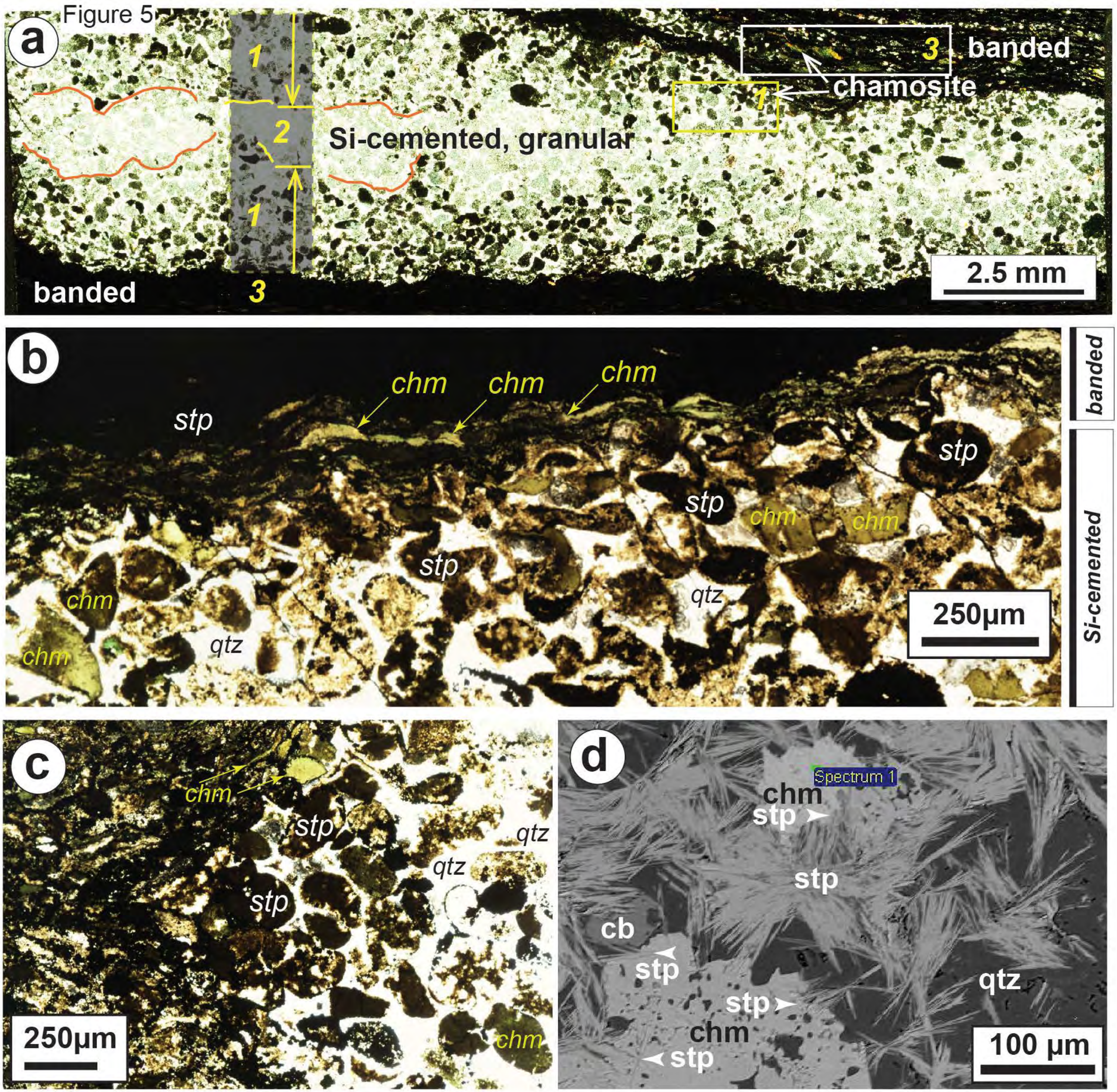
a
1
2
1
3
Si-cemented, granular
banded
banded
3
1
chamosite
2.5 mm
b
chm
chm
chm
stp
stp
stp
stp
chm
chm
chm
chm
qtz
qtz
250µm
banded
Si-cemented
c
chm
stp
stp
qtz
qtz
chm
250µm
d
Spectrum 1
chm
stp
stp
cb
stp
stp
chm
stp
qtz
100 µm

Figure 6

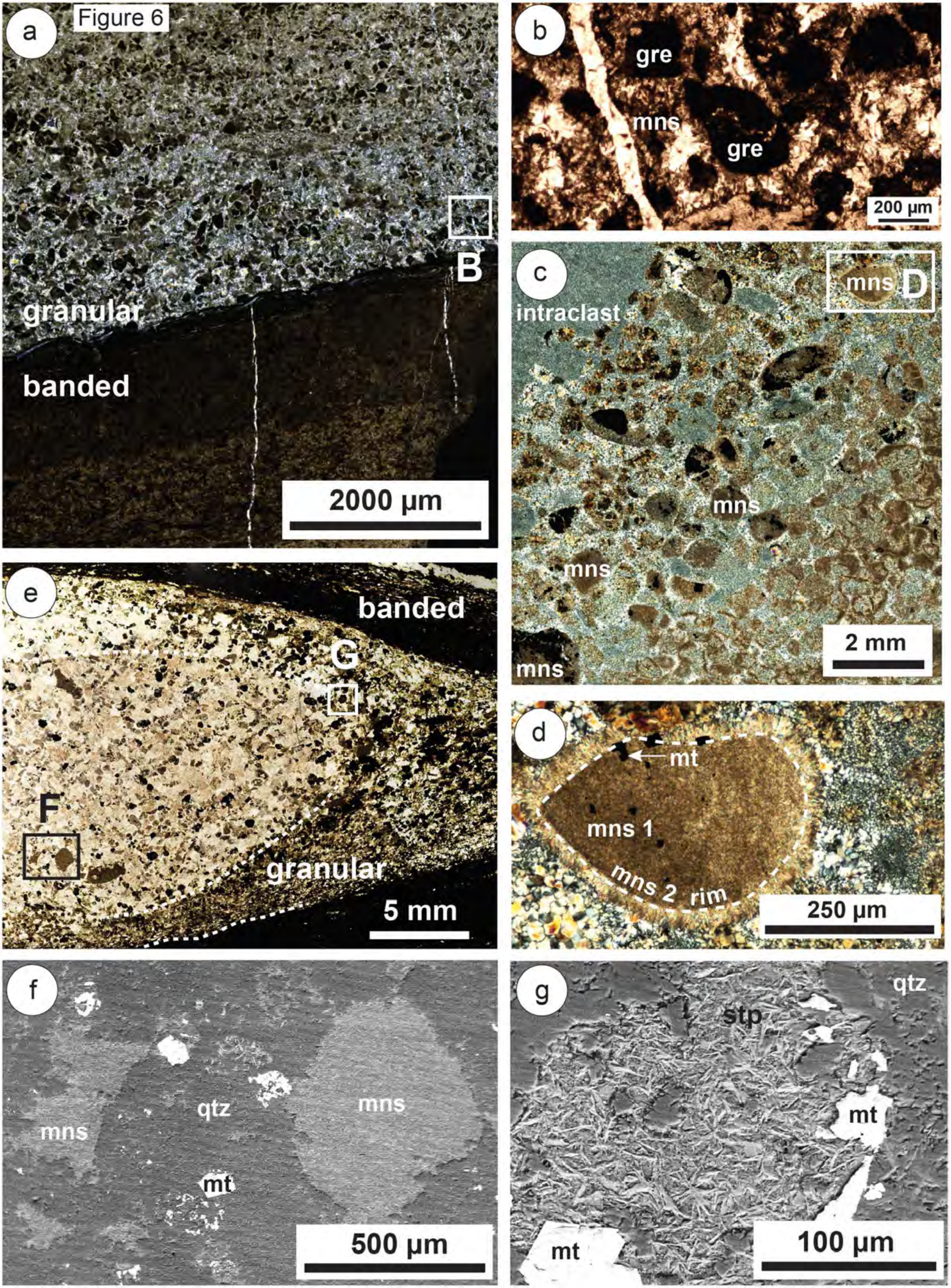
a
B
granular
banded
2000 µm
b
gre
mns
gre
200 µm
c
intraclast
mns
D
mns
mns
mns
2 mm
e
banded
G
F
granular
5 mm
d
mt
mns 1
mns 2 rim
250 µm
f
mns
qtz
mns
mt
500 µm
g
qtz
stp
mt
mt
100 µm

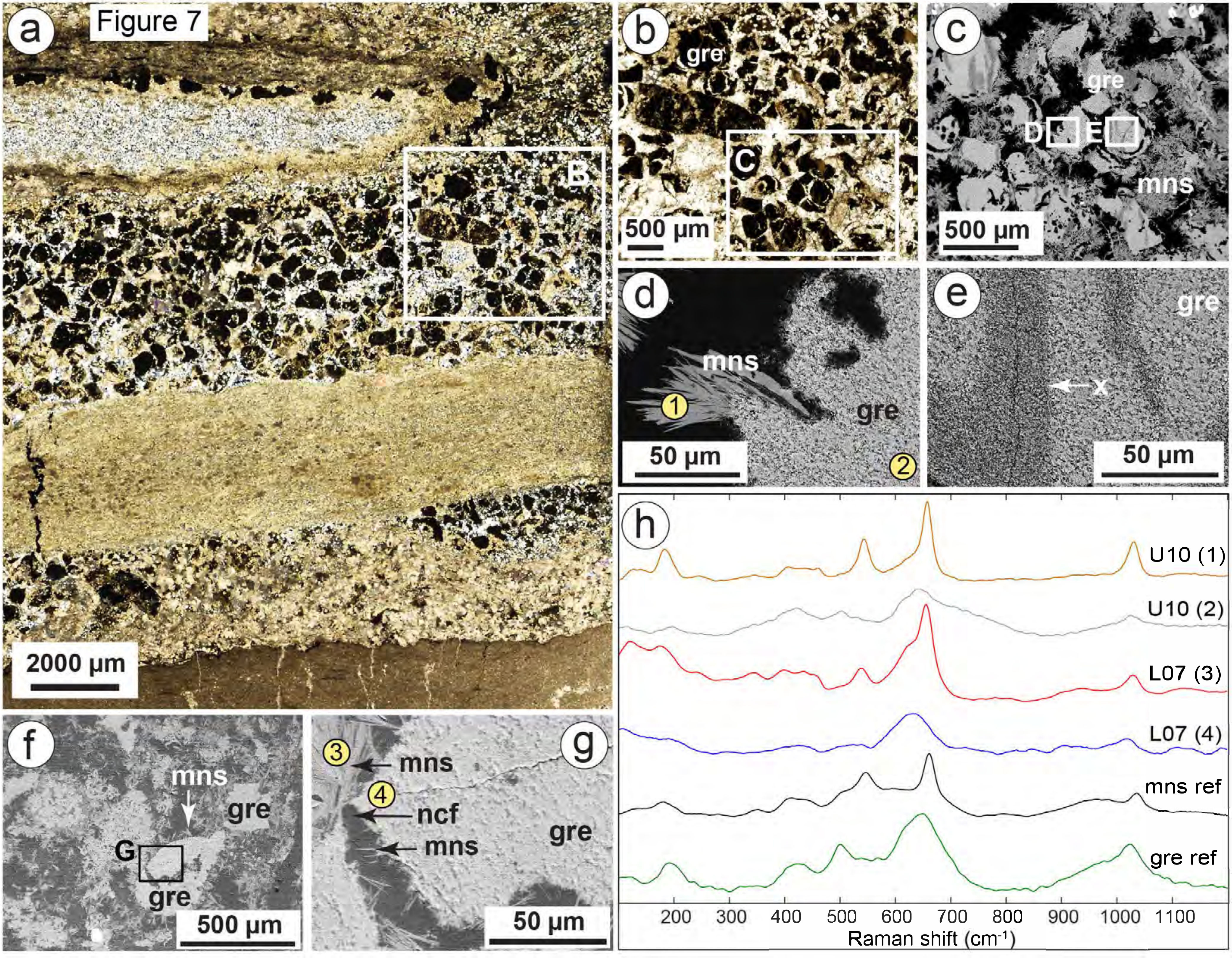

a
Figure 7
B
2000 µm
b
gre
C
500 µm
c
gre
D
E
mns
500 µm
d
mns
1
gre
2
50 µm
e
gre
x
50 µm
f
mns
gre
G
gre
500 µm
g
3
mns
4
ncf
mns
gre
50 µm
h
U10 (1)
U10 (2)
L07 (3)
L07 (4)
mns ref
gre ref
200
300
400
500
600
700
800
900
1000
1100
Raman shift (cm⁻¹)

Figure 8

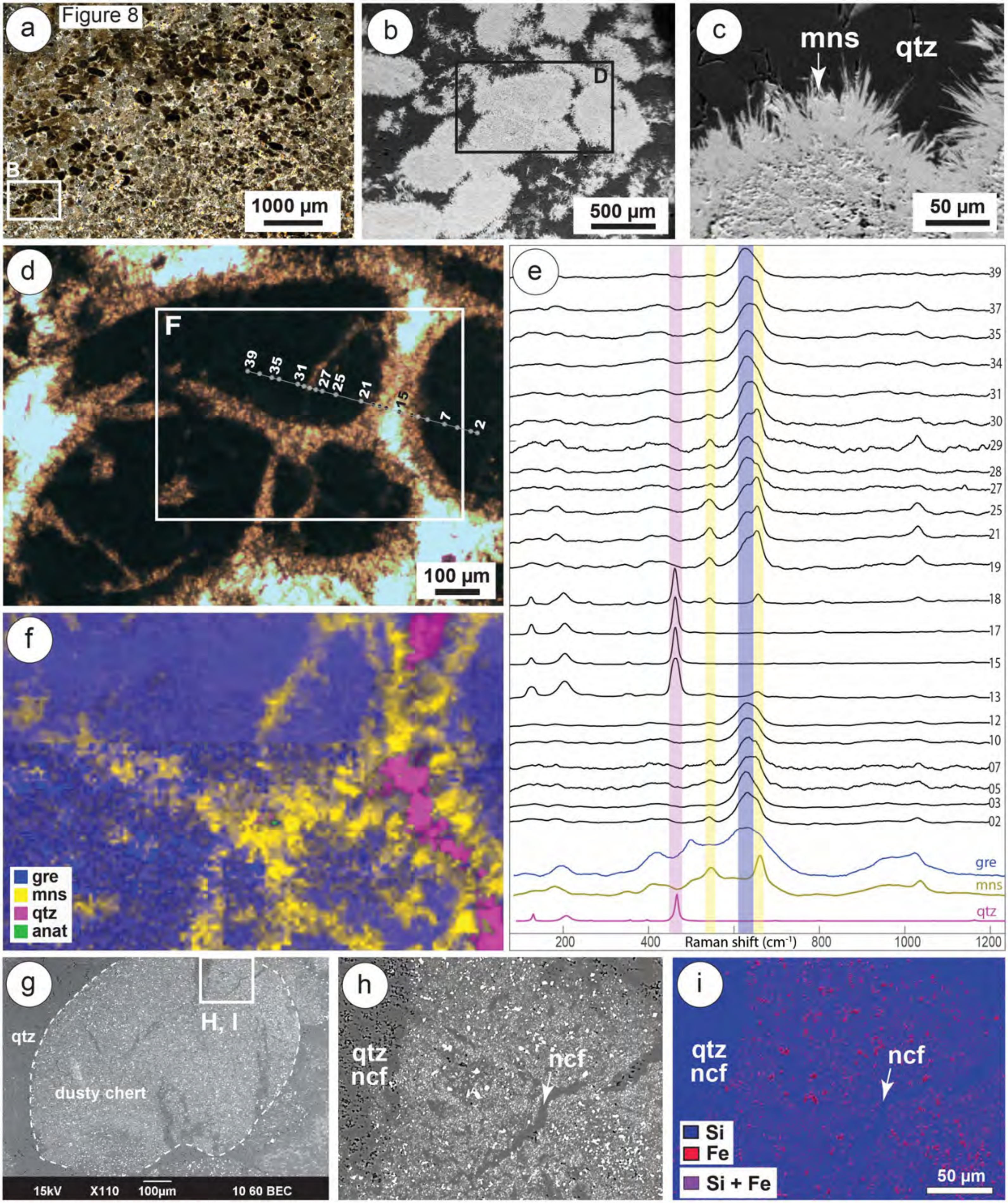
a
B
1000 µm
b
D
500 µm
c
mns
qtz
50 µm
d
F
39
35
31
27
25
21
15
7
2
100 µm
e
39
37
35
34
31
30
29
28
27
25
21
19
18
17
15
13
12
10
07
05
03
02
gre
mns
qtz
200
400
Raman shift (cm⁻¹)
800
1000
1200
f
gre
mns
qtz
anat
g
H, I
qtz
dusty chert
15kV X110 100µm 10 60 BEC
h
qtz
ncf
ncf
i
qtz
ncf
ncf
Si
Fe
Si + Fe
50 µm

Figure 9

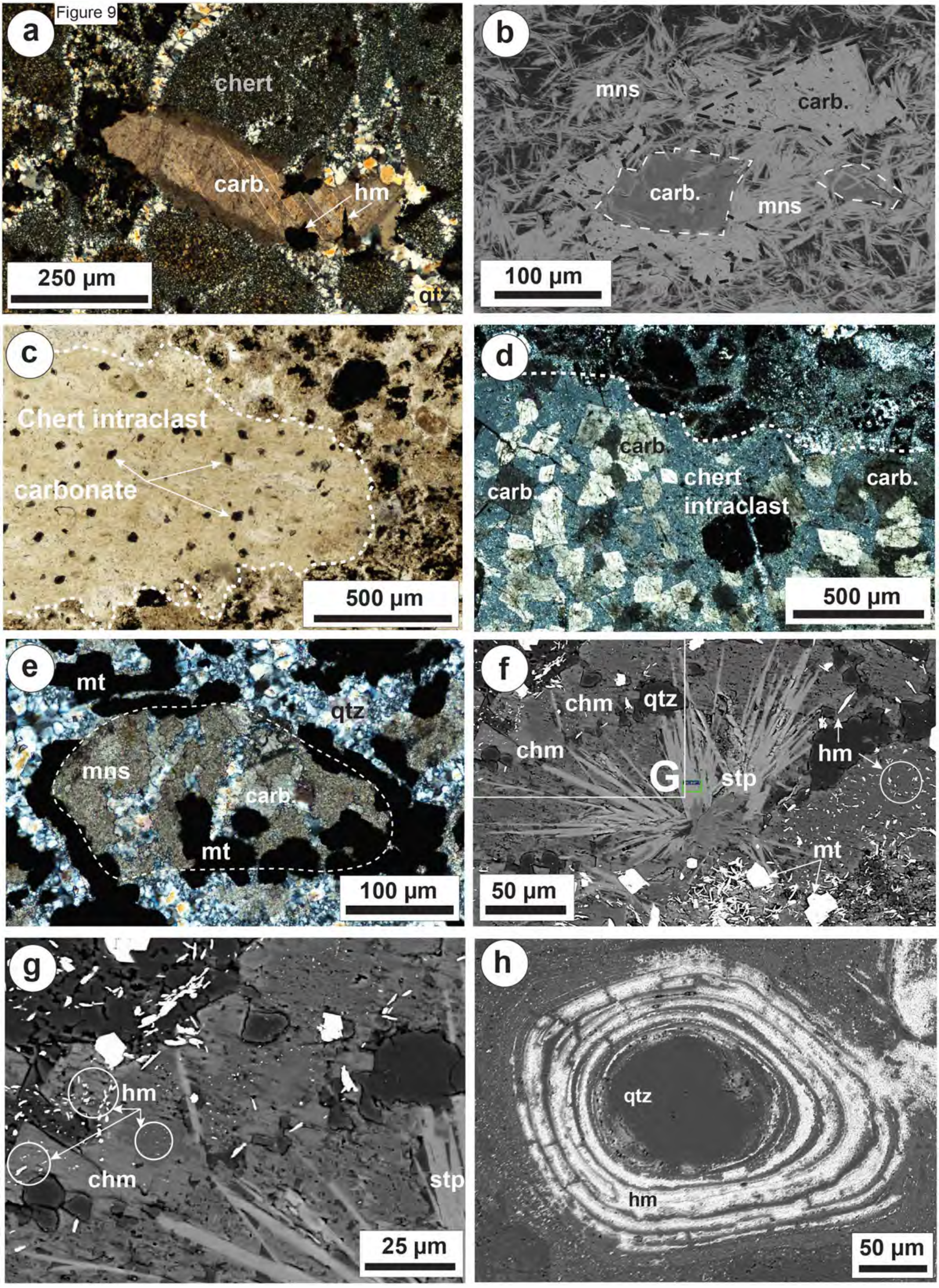
a
chert
carb.
hm
250 µm
qtz
b
mns
carb.
carb.
mns
100 µm
c
Chert intraclast
carbonate
500 µm
d
carb.
chert
intraclast
carb.
carb.
500 µm
e
mt
qtz
mns
carb.
mt
100 µm
f
chm
qtz
chm
G
stp
hm
mt
50 µm
g
hm
chm
stp
25 µm
h
qtz
hm
50 µm

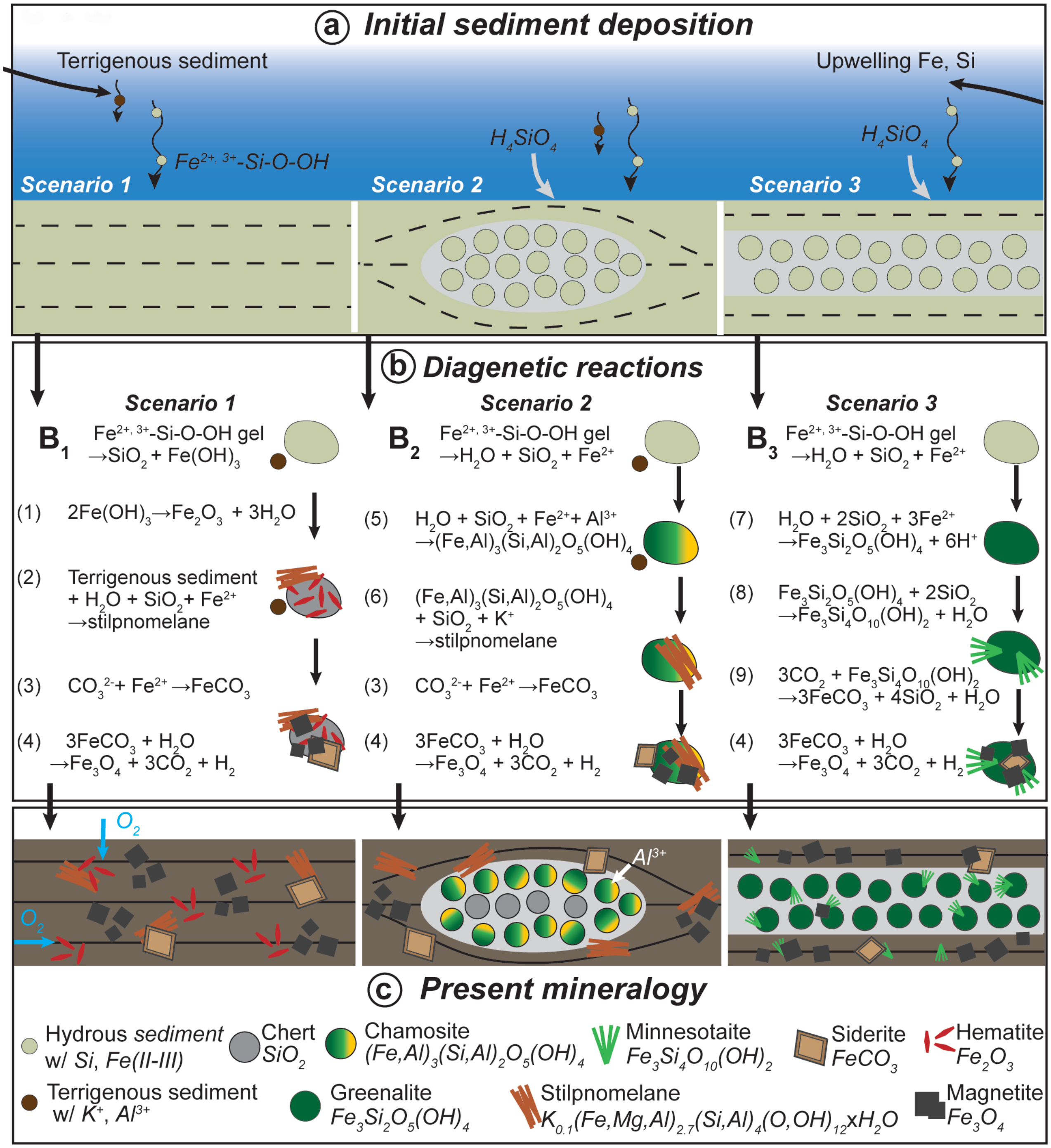
ⓐ Initial sediment deposition
Terrigenous sediment
Upwelling Fe, Si
$Fe^{2+,3+}$-Si-O-OH
H_4SiO_4
H_4SiO_4
Scenario 1
Scenario 2
Scenario 3
ⓑ Diagenetic reactions
Scenario 1
Scenario 2
Scenario 3
B_1 $Fe^{2+,3+}$-Si-O-OH gel $\rightarrow SiO_2 + Fe(OH)_3$
(1) $2Fe(OH)_3 \rightarrow Fe_2O_3 + 3H_2O$
(2) Terrigenous sediment + $H_2O + SiO_2 + Fe^{2+}$ →stilpnomelane
(3) $CO_3^{2-} + Fe^{2+} \rightarrow FeCO_3$
(4) $3FeCO_3 + H_2O \rightarrow Fe_3O_4 + 3CO_2 + H_2$
B_2 $Fe^{2+,3+}$-Si-O-OH gel $\rightarrow H_2O + SiO_2 + Fe^{2+}$
(5) $H_2O + SiO_2 + Fe^{2+} + Al^{3+} \rightarrow (Fe,Al)_3(Si,Al)_2O_5(OH)_4$
(6) $(Fe,Al)_3(Si,Al)_2O_5(OH)_4 + SiO_2 + K^+$ →stilpnomelane
(3) $CO_3^{2-} + Fe^{2+} \rightarrow FeCO_3$
(4) $3FeCO_3 + H_2O \rightarrow Fe_3O_4 + 3CO_2 + H_2$
B_3 $Fe^{2+,3+}$-Si-O-OH gel $\rightarrow H_2O + SiO_2 + Fe^{2+}$
(7) $H_2O + 2SiO_2 + 3Fe^{2+} \rightarrow Fe_3Si_2O_5(OH)_4 + 6H^+$
(8) $Fe_3Si_2O_5(OH)_4 + 2SiO_2 \rightarrow Fe_3Si_4O_{10}(OH)_2 + H_2O$
(9) $3CO_2 + Fe_3Si_4O_{10}(OH)_2 \rightarrow 3FeCO_3 + 4SiO_2 + H_2O$
(4) $3FeCO_3 + H_2O \rightarrow Fe_3O_4 + 3CO_2 + H_2$
O_2
O_2
Al^{3+}
ⓒ Present mineralogy
Hydrous sediment w/ Si, Fe(II-III)
Chert SiO_2
Chamosite $(Fe,Al)_3(Si,Al)_2O_5(OH)_4$
Minnesotaite $Fe_3Si_4O_{10}(OH)_2$
Siderite $FeCO_3$
Hematite Fe_2O_3
Terrigenous sediment w/ K^+, Al^{3+}
Greenalite $Fe_3Si_2O_5(OH)_4$
Stilpnomelane $K_{0.1}(Fe,Mg,Al)_{2.7}(Si,Al)_4(O,OH)_{12}xH_2O$
Magnetite Fe_3O_4